# Active subaquatic fault segments in Lake Iznik along the middle strand of the North Anatolian Fault, NW Turkey

R. Gastineau[1,2], J. de Sigoyer[1], P. Sabatier[2], S.C. Fabbri[3], F.S. Anselmetti[3], AL. Develle[2], M. Şahin[4], S. Gündüz[4], F. Niessen[5] and A. C. Gebhardt[5]

1 Univ. Grenoble Alpes, Univ. Savoie Mont Blanc, CNRS, IRD, IFSTTAR, ISTerre, 38000 Grenoble, France

2 EDYTEM, Université Savoie Mont-Blanc, Université Grenoble Alpes, CNRS, Le Bourget du Lac, France

3 Institute of Geological Sciences and Oeschger Centre for Climate Change Research, University of Bern, Baltzerstrasse 1+3, 3012 Bern, Switzerland

4 Bursa Uludağ Üniversitesi, Fen-Edebiyat Fakültesi, Arkeoloji Bölümü, Görükle, Bursa, Turkey.

5 Alfred Wegener Institute (AWI) Helmholtz Centre for Polar and Marine Research, D-27568, Bremerhaven, Germany

Corresponding author: Renaldo Gastineau (renaldo.gastineau@univ-grenoble-alpes.fr)

**Key points:**

1. Previously unknown faults that belong to the North Anatolian Fault system have been discovered in Lake Iznik through geophysical surveys (from multibeam bathymetry and high-frequency seismic reflection data).

2. Assessment of the recent activity of the Iznik Fault, based on multiproxy analysis of sediment cores from each side of the fault.

3. Evidence for the timing of the last rupture corresponding to the 1065 CE historical earthquake, which had significantly impacted the city of Iznik.

27 **Abstract**

28 The seismic activity of the middle strand of the North Anatolian Fault (MNAF), Northwestern Turkey, is

29 debated because of its quiescence during the instrumental period, in contrast to a significant historical activity

30 documented by several chronicles over the last two millennia. Here, we focus on Lake Iznik, bordered by the

31 MNAF, to get a new insight into its long-term seismicity and its tectonic setting. The study of lacustrine

32 sediment cores reveals fourteen earthquake-induced turbidites since their ages correspond to seismic events

33 during the past two millennia. Bathymetry and high-resolution seismic reflection data allow to describe two

34 hitherto unknown subaquatic active fault structures (the South Boyalica and Iznik faults) that belong to the

35 MNAF system. Sediment cores sampled on both sides of the Iznik Fault document an event deposit and a

36 sedimentary unit vertically offset of ~ 40 cm interpreted as the last rupture during the 1065 CE destructive

37 earthquake. Older events are supposed on this fault more than thousand years ago. Further studies will help

38 to estimate the horizontal coseismic offset of this oblique-slip fault and the calendar of older ruptures. The

39 current seismic gap of thousand years on this segment greatly increases the seismic hazard in this region and

40 must be considered in the seismic risk assessment of the NAF system.

41 **Plain Language Summary**

42 During large earthquakes, sediments are generally transported from lake slopes to the lake basin. The

43 resulting event deposits can provide information on the recurrence of past regional earthquakes, which is

44 crucial for seismic hazard assessment. In this study, we discovered two underwater fault structures in Lake

45 Iznik, using geophysical methods. Studying the sedimentation on both sides of the southernmost fault, we

46 observed an increased sedimentation rate on the hanging wall of the fault immediately after an event deposit,

47 dated to 1077 +/- 77 cal. CE. We interpreted these indicators as resulting from a coseismic displacement

48 along the fault plane, linked to the 1065 CE historical earthquake, which had significantly impacted the city

49 of Iznik. We also show that most of the other event deposits in the sediment cores are confidently associated

50 to 14 historical earthquakes since 2000 years.

## 1. Introduction

Earthquakes are the costliest and deadliest natural events in Turkey with about 100,000 deaths in the last century (Öcal, 2019). Despite their lower frequency compared to other events such as floods, the impact of earthquakes cannot be ignored in this densely populated part of the world. The seismic hazard in the northwestern part of Turkey is mainly linked to the North Anatolian Fault (NAF), a 1500 km-long right-lateral strike-slip fault, which accommodates the westward migration of the Anatolian microplate, away from the Eurasian/Arabian collision (Reilinger et al., 2006).

In its western termination, the NAF zone displays a complex organization as it is divided into three branches (**Fig. 1**). Its northern strand (NNAF) continues south of Istanbul through the Marmara Sea (e.g. Armijo et al., 2005). Its middle strand (MNAF) borders the south of two successive basins, known as the Geyve-Pamukova Basin and the Iznik Basin, which hosts Lake Iznik and continues through the Gemlik Bay to the southern shore of the Marmara Sea (**Fig. 1**). Its southern strand (SNAF) is less pronounced in the landscape and extends across the Bursa Province (**Fig. 1**). With a relative horizontal motion estimated around 5 mm/yr by GPS (Ergintav et al., 2014), both MNAF and SNAF show a deformation rate 5-fold smaller than the NNAF (~ 25 mm/yr) (Reilinger et al., 2006). This is also reflected by the recent seismicity of the NAF: from 1939 to 1999, a sequence of great earthquakes (moment magnitude Mw > 6.8) shifted westward from Erzincan to Düzce and Izmit (**Fig. 1**; Stein et al., 1997). The last major earthquake on the NNAF occurred in 1999 along the Izmit-Sapanca rupture and was a 7.6 Mw event. A ground-motion study revealed that this fault segment broke with a supershear velocity during the earthquake (Bouchon, 2002). This destructive event caused extensive liquefaction-induced ground deformation on the shores of Lake Sapanca triggering the submergence of a hotel (Cetin et al., 2002). The succession of the earthquakes on the NNAF is explained by the cumulative Coulomb stress along the fault (Stein et al., 1997). According to this concept and several studies with complementary methods, a seismic gap is inferred on the NNAF segment in the Marmara Sea, which was seismically inactive since the 18th century (Hubert-Ferrari et al., 2000). This future rupture may lead to a Mw > 7 earthquake and strike Istanbul (e.g. Parsons, 2000; Armijo et al., 2005; Bulut et al., 2019; Lange et al., 2019). However, these different models only encompass the recent seismicity (since 1700 CE) on the NNAF branch, but do not take into account either the MNAF or the SNAF. While the NNAF produced several major earthquakes since that time (Ambraseys, 2002), the SNAF produced a 7.3 Mw earthquake in 1953 and a 6.9 Mw earthquake in 1964 (Ambraseys, 2002). However, no major earthquake ruptured on the

82    MNAF for several centuries, and a very low seismicity has been recorded during the instrumental period.

83    The last big earthquake on the MNAF may have occurred between the 14th and 18th centuries CE (Ambraseys,

84    2002). This long quiescence strongly contrasts with a significant historical tectonic activity on the MNAF.

85    Several chronicles and archaeological studies report the partial destruction of the city of Iznik (previously

86    called Nicaea) and surrounding areas following ~ 15 major earthquakes within the last 2000 years with

87    unknown rupture segments (Ambraseys & Finkel, 1991; Ambraseys & Jackson, 2000; Ambraseys, 2002;

88    Benjelloun et al., 2020). The quiescence of the MNAF in recent times may hide a longer seismic recurrence,

89    which possibly is just as hazardous as the NNAF (according to their span of quiescence), but has been

90    underestimated by the models. This study aims to specify the earthquake catalogue in the Iznik area to

91    determine the seismic cycle of the MNAF and to provide new data for the tectonic setting of this fault strand.

92    This study is the first to use the sedimentary record of the Lake Iznik to document past earthquakes along the

93    MNAF. It complements previous studies done close to different fault segments of the NNAF in different sub-

94    basins of the Marmara Sea through sediment analysis (e.g. McHugh et al., 2006; Çağatay et al., 2012; Drab

95    et al., 2012; Eriş et al., 2012). It will bring new paleoseismic informations in this region.

96    Lake sediments are continuous archives used to reconstruct past earthquake history (Monecke et al., 2004;

97    Strasser et al., 2006; Beck, 2009; Strasser et al., 2013; Van Daele et al., 2015; Avşar et al., 2015; Wilhelm et

98    al., 2016; Moernaut et al., 2017; Rapuc et al., 2018). Compared to historical and terrestrial archives, lake

99    sediments provide a complementary and more continuous paleoseismic record (e.g. Strasser et al., 2013;

100   Wilhelm et al., 2016). Combining on-fault studies such as trenching with studies investigating earthquake-

101   induced turbidites in lakes not only provides direct evidence for fault displacement in the case of surface

102   ruptures (e.g. Beck et al., 2015), but also allows to document seismic events off-fault without surface ruptures

103   (Brocard et al., 2016). We propose here to investigate Lake Iznik using a combined geophysical and

104   sedimentological approach to provide new insights into the seismicity of the Iznik region over the past

105   millennia. These methods have been already used on submarine ocean-floor faults such as in the Marmara

106   Sea or in the Lesser Antilles (e.g. Armijo et al., 2005; Beck et al., 2012; McHugh et al., 2014).

## 2. Context

### 2.1 Geological settings and previous studies on the MNAF

The NAF originated some 11-13 Ma ago within a wider pre-existing shear zone, which became progressively narrower through time (Şengör et al., 2014). While most of NAF segments are known to have a right-lateral kinematics, several segments show oblique (transtensional) kinematics with local deformation partitioning between right-lateral strike-slip and extensional regimes (Kurt et al., 2013; Doğan et al., 2015; **Fig. 2**). The origin of the Iznik Basin is still under debate: it has been interpreted as a superimposed basin evolved due to the intersection of the younger NAF and the Thrace Eskişehir Fault (Yaltırak, 2002; Öztürk et al., 2009) or as a more complex transtensional basin due to MNAF activity (Doğan et al., 2015). The geological inheritance is reflected by the relatively high lithological heterogeneity and tectonic complexity within the watershed (**Fig. 2a**). The Gürle Fault (a segment of the MNAF) has a normal component (Doğan et al., 2015), which explains the current location of the deepest depocentre of Lake Iznik (~ 75 m depth b.l.l.; **Fig. 2a**). This normal component is also expressed by the 100 m-high triangular facets on Lake Iznik's southern shore (**Fig. 2b**). Fault partitioning thus certainly exists; whereas the onshore Gürle Fault accommodates most of the normal component, another fault segment should somewhere accommodate the dextral component (**Fig. 2b**).

At least fifteen earthquakes were documented in historic chronicles in Iznik during the last two millennia, (Ambraseys & Finkel, 1991; Ambraseys & Jackson, 2000; Ambraseys, 2002; Benjelloun et al., 2020). According to these archives, the epicenter of some of them is located on the MNAF (29-32; 121; 368 and 1065; the 1419 CE earthquake was also recorded on the SNAF so the epicenter location is still under debate). More than 20 trenches carried out on different segments of the MNAF confirmed its activity (e.g. Honkura & Işikara, 1991; Barka, 1993; Uçarkuş, 2002; Doğan, 2010; Özalp et al., 2013; see **Fig. 2a** for their locations). One to three ruptures were identifying on them but very few of them gave reliable ages. It is therefore difficult to conclude on the precise rupture ages on the different segments of the MNAF, and on their earthquake recurrence rate. The city of Iznik hosts many archeological remains affected by past earthquakes, such as the recently discovered submerged basilica in Lake Iznik (Şahin, 2014; Şahin & Fairchild, 2018). Through a systematic survey of Earthquake Archeological Effects (EAE) on Iznik's buildings, Benjelloun et al., (2020) showed that three damage episodes are recorded: between the 6th and late 8th centuries CE, between the 9th and late 11th centuries CE and after the late 14th century CE. The second

136  episode is clearly related to an earthquake in 1065 CE that was well described in many local chronicles and

137  caused several damages in Iznik, whereas the two other episodes could be explained by different earthquake

138  scenarios.

139          **2.2 Lake catchment**

140  Lake Iznik (83.5 m a.s.l, 40°26'N, 29°32'E), formerly known as Lake Askania, is located southeast of the

141  Marmara Region (Bursa Province), east of the Gemlik Bay (**Fig. 1**). It is the fifth-largest lake of Turkey, and

142  the largest of the Marmara Region with a N-S and E-W extent of 12 and 32 km, respectively (**Fig. 2a**). The

143  lake has a catchment area of ~ 1257 km² and a surface area of 313 km². The watershed shows a heterogeneous

144  geology, with a northern part relatively rich in volcanic, metamorphic rocks and carbonates, while the

145  southern part is mostly composed of siliciclastic sediments with only sporadic carbonate and volcanic

146  sections. Iznik has been an important city throughout history. Different archaeological excavations in the

147  area suggest that the first farming activities began 6000-5400 BCE (Roodenberg, 2013). Since the first

148  humans settled in the watershed, the land has been cultivated: cereals, olives, and walnuts were among the

149  most important crops in the Iznik area (Miebach et al., 2016). The lake is peanut-shaped with a non-regular

150  shoreline (**Fig. 2a**). A rough bathymetry of the lake, assembled by the General Directorate of Turkish

151  Hydraulic Works (DSI), shows that the lake comprises three sub-basins, reflecting its tectonic complexity

152  (**Fig. 2a**). One isolated sub-basin is located in the western part of the lake, whereas two sub-basins form the

153  central and eastern parts, with one in the North and the deepest one in the South separated by a E-W elongated

154  ridge (**Fig. 2a**). The main inflows are the Sölöz, Nadir, Kuru, Kara and Kiran rivers (**Fig. 2a**). The only outlet

155  of the lake is the Karsak River, which discharges the waters westward to the Marmara Sea through the Gemlik

156  Bay. The Iznik Basin is bordered by two mountain ranges: The Samanli Mountains (max. elevation 1227 m

157  a.s.l.) to the North, and the Katırli Mountains to the South (1275 m a.s.l.) (**Fig. 2a**). Previous studies of Lake

158  Iznik's sediments have provided an up to 36 kyr-long paleoclimatic archive (Roeser et al., 2012; Ülgen et al.,

159  2012; Viehberg et al., 2012; Miebach et al., 2016). In these past studies of Lake Iznik's sedimentary archives,

160  no event deposits (except tephra layers), were identified in the sedimentary sequence.

## 3. Methodology

### 3.1 Bathymetry

The bathymetric survey was completed in April 2019 using a fishing boat with a Kongsberg EM2040 multibeam echosounder (Kongsberg Maritime, Horten, Norway, provided by University of Bern) in a single-head configuration (1° by 1° beam width, 300 kHz standard operating frequency; 400 depth detections per ping). The angular coverage was 148° maximum, with a coverage of up to ~ 3 times water depth on a flat bottom. The transducers and auxiliary sensors Kongsberg Seatex MRU5+ motion sensor (Kongsberg Seatex, Trondheim, Norway), a Trimble SPS361 heading sensor (Trimble Navigation Limited, Sunnyvale, CA, USA), a Leica GX1230 GNSS receiver (Leica Geosystems, Heerbrugg, Switzerland) using the TUSAGA Aktif GEO real-time positioning service (national active fixed GNSS, Turkey; typical position accuracy 2 to 3 cm) and a Valeport MiniSVS sound velocity sensor (Valeport Limited, Totnes, UK) were used. The transducers, motion sensor and mini sound velocity sensor were incorporated in a rigid mounting attached to the bow of the ship. The ship speed ranged from 7-9 km/h.

The vertical sound velocity in the water column was recorded daily by a Valeport Sound Velocity Profiler (SVP) that recorded pressure, temperature and the sound velocity in the water column. Sound velocity depends on the temperature and the salinity of the water. The absolute depth accuracy depends on the correctness of the water velocity profiles, the motion sensor's capability to compensate for ship movements due to waves, positioning accuracy, the water depth and is in the range of centimeters (shallow waters) to a few decimeters (>50 m depth). Data were recorded using Kongsberg's SIS software and processed in HIPS/SIPS 10.4.13 software (University of Bern), then interpreted using ArcGIS 10.4.1.

### 3.2 Seismic acquisition

The seismic profiles were acquired using a 3.5 kHz system (Geopulse, Geoacoustic) in 2005 with a single-channel streamer (20-elements AE5000, GeoAcoustics) and an array of four sub-bottom profiling transducers (Mod. TR-1075A, Massa, USA) as receivers. Shot interval was 1 second. For navigation, a 3x4 m UWITEC aluminum platform ("R/V Helga") equipped with 4 inflatable tubes for flotation and a 25 HP outboard engine were used. The average speed of the vessel was 5 km/h. All 3.5 kHz data were digitized (Octopus 360, Octopus Marine Systems, UK) and processed (15 to 5000 Hz filtering) using Reflex software (Sandmeier Software, Germany). All profiles were interpreted using IHS Markit® Kingdom v.2015.

189      **3.3 Coring and lithological description**

190      Five short cores (registered in the French national cyber-core-repository https://www.cybercarotheque.fr and

191      the open international database www.geosamples.org as IZN19_03 (1.37 m; IGSN: TOAE0000000310),

192      IZN19_04 (1.60 m; IGSN: TOAE0000000311), IZN19_16 (1.25 m; IGSN: TOAE0000000322), IZN19_21

193      (2.70 m; IGSN: TOAE0000000297) and IZN19_31 (2.79 m; IGSN: TOAE0000000307)) were collected from

194      Lake Iznik in April and July, 2019, using a UWITEC gravity corer with hammering. The cores were sampled

195      on strategic points, depending on the first bathymetric and seismic results. In the laboratory, the cores were

196      split into two halves. Each core was photographed after oxidation and a detailed sedimentological description

197      was performed. The lithological description of the sequences allowed the identification of different

198      sedimentary structures and facies, which were then correlated between the cores. Colors were assigned

199      according the Munsell's color chart (Munsell Color, 1994).

200      **3.4  Sedimentological analysis**

201      **Grain-size analysis**

202      The grain-size distribution of the sediment was determined following a mean of 5 cm sampling step all along

203      the longest sequence (IZN19_21; **Fig. 3** for location). As the sequence contains sporadic mm-thick sandy

204      deposits, the resolution in these parts was increased to 0.5 cm. A Beckman Coulter Life Science 13 230 XR

205      laser particle-size analyzer was used (EDYTEM Laboratory, University Savoie Mont Blanc) with sonication

206      to avoid particle flocculation. Two runs with a 30s-long measurement were applied for each fresh sample.

207      Results of the grain-size distribution were processed with MATLAB R2016b software and presented in a

208      contour plot with a color-scale according to the abundance of particles in percentage for each grain-size class.

209      **Scanning Electron Microscopy (SEM) and Energy-Dispersive Spectroscopy (EDS)**

210      To complete the core description, a representative 8 cm-long slab including two coarser-grained deposits was

211      resin-embedded to make 1 mm-thick thin sections of the sediment, which were analyzed with a Vega3 Tescan

212      Scanning Electron Microscope (ISTerre Laboratory, University Grenoble Alpes) following covering with a

213      graphite layer of 20 nm. Representative areas of the thin section were additionally analyzed with an Energy-

214      Dispersive Spectroscopy (EDS) probe (Rayspec with SamX's electronic system and software, ISTerre

215      Laboratory) to examine the elementary composition and to map chemical elements on specific lamina.

**Loss on ignition**

The loss on ignition (LOI) analysis was performed on the IZN19_31 sequence (**Fig. 3** for location), with a 10-cm sampling interval all along the sequence to estimate organic matter (OM) and carbonate proportion in the sediment, following the protocol described by Heiri et al., (2001).

### 3.5 Geochemistry

The relative contents of major and trace elements were analyzed with an X-Ray Fluorescence (XRF) at 1-mm resolution on the surface of each sediment core with an Avaatech Core Scanner (EDYTEM Laboratory). The split core surface was first covered with a 4-μm-thick Ultralene film to avoid contamination and desiccation of the sediment. Element intensities are expressed in counts per second (cps). Different settings were used with 10 kV and 0.2 mA during 15 s to detect Al, Si, S, K, Ca, Ti. and at 30 kV and 0.3 mA during 20 s for Mn, Fe, Ni, Cu, Zn, Br, Rb, Sr, Zr, Pb (Richter et al., 2006). A Principal Component Analysis (PCA) was performed on the geochemical results using R software version 3.5.1 (R Core Team, 2018) to determine correlations between the different measured elements and to identify principal sediment end-members, which are used to better constrain each sedimentological facies (e.g. Sabatier et al., 2010).

### 3.6 Chronology of the cores

Eleven $^{14}$C analyses of eleven organic plant macro remains were performed by accelerator mass spectrometer (AMS) at the Poznan Radiocarbon Laboratory. The $^{14}$C ages were calibrated using the Intcal20 calibration curve (Reimer et al., 2020). Calibrated ages are expressed in the Common Era (CE) timescale: years before the CE are denoted BCE (Table 1). The age model and the sedimentation rate were calculated using the R code package *clam* (Blaauw, 2010). The best fit was obtained by applying a smooth spline model with 0.35 and 0.40 for the smooth parameter (for IZN19_21 and IZN19_31 cores respectively).

## 4. Results

### 4.1 Lake Bathymetry

One third of the surface area of Lake Iznik (~ 80.5 km²), was mapped in high-resolution (**Fig. 2a**). Two prominent lineaments were discovered on the bathymetric data. One is located to the north, parallel to the onshore Boyalıca Fault and strikes NE-SW. This lineament separates the northern sub-basin and the shoreward underwater terraces (**Fig. 3c**).

243    The other lineament, striking NW-SE, has been discovered on the southeastern part and mapped over a

244    distance of 9 km (**Fig. 3a**). It separates the southern sub-basin from the central ridge (**Fig. 2**) in the middle of

245    the lake. This lineament presents two kinks separating it into three segments: IFS1, IFS2 and IFS3 (**Fig. 3a***)*.

246    IFS1 and IFS3 are ~ 3 km length (**Fig. 3a**). The bathymetric profile perpendicular to the IFS1 shows a ~ 1 m

247    vertical offset of the lake floor (profile P1; **Fig. 3d**), extending over a distance of ~ 100 m. These segments

248    are linked by IFS2 those scarp is barely visible on the bathymetric data (**Fig. 3a**). Furthermore, numerous

249    pockmarks are visible along the fault trace at the transition from IFS2 to IFS3, indicating fluid escapes (**Fig.

250    3b**). The size of these depressions varies from few centimeters to 6 m diameter and reaches ~ 60 cm deep

251    (**Fig. 3d**). Where the lineament extends ashore, it merges into the main branch of the MNAF, close to the

252    village of Dırazali. However, the surface expression of the fault is masked by human activity, mainly due to

253    fields of olive and fruit trees. According to these observations, we interpreted this lineament as a fault, termed

254    Iznik Fault.

255        **4.2 Seismic reflection data**

256    High-resolution seismic profiles were acquired across IFS2 and IFS3 (**Fig. 3a**). These single-channel

257    reflection sections show maximum acoustic penetration of ~ 10 ms two-way travel time or ~ 7.5 m (assuming

258    acoustic velocities of 1500 m/s), after which signals become weaker and difficult to interpret due to high gas

259    content of the sediment. Chaotic-to-transparent acoustic seismic facies is interpreted as turbidite deposits or

260    mass-movement deposits indicating a slope failure at the location of IFS3 on the seismic section supporting

261    the fault nature of the lineament and its location (Profile P2; **Fig. 4**) (e.g. Cukur et al., 2013). Although it is

262    difficult to assess the vertical offset on the different seismic profiles, the continuity of the seismic reflections

263    is affected across the fault. The second seismic section parallel to IFS2 (Profile P3; **Fig. 4**), does not show

264    any clear slope failure but only slight vertical offsets of the seismic reflections and a series of closely-spaced

265    incipient faults displacing steeply the uppermost meters of sediment.

266        **4.3 Sedimentary sequences**

267    **Sedimentary facies**

268    Lake Iznik sediments consist mainly of clays and silts (Roeser et al., 2012; **Fig. 5**). In the here investigated

269    short cores, very fine to fine sand laminae appear very sporadically at the millimeter scale in the finer matrix

270  of background deposits. Based on macroscopic observations and confirmed by geochemical analysis, four

271  main lithological facies were identified.

272      -    Facies I is composed of brown (5Y/4/4) silt (D50 = 10 µm) and occurs at the top of each core. The

273           organic proportion (LOI550) of this facies amounts to ~ 9 % and the carbonate proportion (LOI950)

274           to 6 %.

275      -    Facies II occurs at different depths in the sequences and consists of slightly coarser light brown

276           (2.5Y/5/4) silt (D50 = 15 µm). Facies II has the highest proportion of organic matter (~ 10 %) and

277           carbonate (~ 10 %).

278      -    The majority of the sedimentary sequence consists of Facies III, which is a more heterogeneous

279           facies with olive grey color (5Y/6/2) clayey silt (D50 = 8 µm). This facies is interrupted by a total

280           of 15 and 18 few-mm-thick (max 2 cm-thick) silt (to sandy) laminae in cores IZN19_31 and

281           IZN19_21, respectively, denoted as Facies IV and termed 'event deposits' (D50 = 20 µm in general).

282           This facies shows the lowest proportion in organic matter (~ 7 %) and carbonates (~ 7 %).

283           Nevertheless, LOI values do not vary much over the entire sequence. The fraction of non-carbonate

284           ignition residue (NCIR) is higher than 80 % for the whole sequence (**Fig. 5a**). All event deposits

285           appear to the naked eye as mm-thick levels of very fine sand or silty lenses within the continuous

286           sedimentation of Facies III. The detailed SEM observations show that these sandy laminae have an

287           erosive base incising into clayey sediments and a fining-upward trend. Bioturbation with vertical

288           burrows is present throughout their base. Burrow length varies from 1 to 4 mm, and they are filled

289           with particles to the overlying laminae (**Fig. 5c**). Moreover, a comparison of the oxide composition

290           of two event deposits compared to the background sedimentation has been performed with the EDS

291           sensor (**Fig. 5c**). These maps show that Facies III and IV have the same major element compositions

292           and that all carbonates within the Facies IV are sometimes composed by Ca and Mg and reach 50

293           µm (**Fig. 5c**). Facies IV laminae are thus distinct from Facies III due to their fining-upward trends,

294           their erosive base and the coarse-grained Ca/low-Mg-carbonates (**Fig. 5***)*.

295  **Geochemistry**

296  PCA was conducted on the XRF geochemical data of both IZN19_31 and IZN19_21 cores located on both

297  sides of the fault (**Fig. 5b**). Dimensions 1 and 2 (denoted as Dim 1 and Dim 2) explain 85.17% and 80.12%

298  of the total variability for IZN19_31 and IZN19_21 cores, respectively. From the variables factor map, two

299     end-members could be identified. The first one, denoted as "terrigenous", shows high positive loadings with

300     Dim 1 (e.g. Al, Si, Ti, K, Rb; in green in **Fig. 5a, b**). The second end-member is interpreted as "in-lake

301     processes" (Ca, Sr, Br). It displays negative loadings on Dim 1 and positive loadings on Dim 2 (red in **Fig.**

302     **5a, b**). We link it to the endogenic carbonate production and organic matter (Guevara et al., 2019). The

303     individual factor map highlights the characteristics of each facies. Facies II is dominated by the endogenic

304     process end-member, which correspond the higher LOI550 values (**Fig. 5b**). In contrast, Facies III is

305     influenced by terrigenous input. Facies I is in an intermediate position with relatively higher Ti counts than

306     Facies II (**Fig. 5a**). Facies IV shows a similar geochemical characteristic and are nearly always occurring

307     within the Facies III (**Fig. 5c**).

308     **Core-to-core correlation**

309     On the basis of the lithological description and XRF measurements, a correlation between the cores across

310     the Iznik Fault is proposed (**Fig. 6***). The IZN19_03 Core has been excluded from the comparison to limit

311     uncertainties because of its distance to this transect (IZN19_03 Core is presented **Figure S1** in the supporting

312     information). On **Fig. 6**, the Dim 1 (terrigenous supply vs. in-lake processes) and the Ca signal are displayed

313     to highlight the stratigraphic units' correlation. Five different stratigraphic units (from top to bottom: purple,

314     green, orange, dark blue, grey) were correlated on the P1 profile across IFS1 (**Fig. 3d**). Thickness of these

315     units varies significantly, particularly between cores in the immediate vicinity of the fault, IZN19_31 on the

316     hanging wall and IZN19_21 on the footwall of the fault. Based on the stratigraphic correlation, it was possible

317     to correlate the radiocarbon dates (**Table 1**) to IZN19_21 and IZN19_31 cores and use all of them for age

318     modeling.

319         **4.4 Radiocarbon dating and age models**

320     Eleven organic terrestrial plant macroremains were dated (**Table 1**) and stratigraphically correlated between

321     cores IZN19_31 and IZN19_21. This allowed us to use all dates on both cores for age modeling (**Fig. 7**).

322     Both cores have almost the same length (279 cm and 270 cm, respectively) and they were taken very close

323     one to the other (200 m apart) on each side of the fault. The core located north of the fault (IZN19_21) spans

324     a larger period of time and reach at the base ~ 640 cal. BCE, whereas the core south of the fault (IZN19_31)

325     encompasses a shorter time period with the base reaching ~ 210 cal. CE. These different basal ages clearly

326     document the higher sedimentation rates south of the faults. Core IZN19_31 shows more pronounced

327     variations in the sedimentation rate, and four periods can be differentiated (**Fig. 7**). (1) a period with a

328    relatively high sedimentation rate from 200 to 350 cal. CE. During this period, the sedimentation rate is

329    almost constant (~ 1.8 mm/yr); (2) The sedimentation rate show a significant increase from 350 to 600 cal.

330    CE reaching 5.6 mm/yr; (3) The sedimentation rate decrease at 0.7 mm/yr around 1300 cal. CE; and (4)

331    Sedimentation rate increases from 1300 cal. CE until the modern period (1.1 mm/yr at the top). Core

332    IZN19_21 shows almost the same trends, but with less pronounced variations (**Fig. 7**).

333

| Sample name | Core | MCD (cm) | Radiocarbon age (yr BP) | Age cal BCE/CE 2σ range | Sample type |
|---|---|---|---|---|---|
| **Poz-118626** | IZN19_03 | 68 | 1170 +/- 35 | 772 – 977 CE | Plant remains |
| **Poz-118628** | IZN19_03 | 122.5 | 1555 +/- 30 | 429 – 579 CE | Plant remains |
| **Poz-118629** | **IZN19_03** | **136** | **1460 +/- 230** | **63 – 1032 CE** | **Plant remains** |
| **Poz-118561** | IZN19_16 | 68.3 | 1205 +/- 30 | 704 – 941 CE | Plant remains |
| **Poz-118973** | IZN19_21 | 70.5 | 1345 +/- 30 | 643 – 775 CE | Plant remains |
| **Poz-118627** | IZN19_21 | 245.5 | 2385 +/- 30 | 719 – 393 BCE | Plant remains |
| **Poz-118972** | IZN19_31 | 82.7 | 1015 +/- 30 | 987 – 1153 CE | Plant remains |
| **Poz-118562** | IZN19_31 | 97.8 | 1070 +/- 30 | 893 – 1026 CE | Plant remains |
| **Poz-118563** | **IZN19_31** | **229** | **1700 +/- 30** | **254 – 419 CE** | **Plant remains** |
| **Poz-118570** | IZN19_31 | 273.5 | 1820 +/- 30 | 130 – 326 CE | Plant remains |
| **Poz-122240** | IZN19_04 | 93 | 515 +/- 30 | 1328 – 1447 CE | Plant remains |

334    *Table 1: Radiocarbon ages for the Lake Iznik sediment cores, in bold the rejected age for age model*

335    *computation. BP denotes Before Present, i.e. before 1950 CE. MCD denotes Meters Composite Depth.*

336    **5.  Discussion**

337        **5.1 Event deposits versus seismic historical archives**

338    The LOI analysis of the cores shows that almost 80% of the whole sediment sequences are composed of

339    terrigenous siliciclastic constituents (**Fig. 5a**), whereas the in-lake carbonate production represents only a

340    minor fraction. Roeser et al., (2014, 2016) showed that Sr is strongly correlate to aragonite, which is closely

341    linked to endogenic precipitation in Lake Iznik's water. In contrast, calcite is linked to both endogenic and

342    detrital input. The terrigenous component is expressed by high Ti counts, which are characteristic of

343 siliciclastic and felsic volcanic rocks in the southern part of the catchment (**Fig. 2a; Fig. 5a, b**). Our study

344 reveals evidence for multiple thin Ti-rich sandy normally graded laminae termed event deposits (Facies IV

345 in **Fig. 5**). The turbidites are defined by their lithological and textural characteristics. They show fining-

346 upward patterns and a higher content of terrigenous elements as indicated by the Ti/Ca ratio and the PCA

347 (**Fig. 5a, b**). Moreover, they show higher values of detrital carbonates shown by the Ca/Sr ratio and the

348 presence of low-Mg coarse-grained carbonates (**Fig. 5a, c**).

349 Turbidites can be triggered by several processes such as hyperpycnal flows related to river flooding (e.g.

350 Wilhelm et al., 2015), remobilization of superficial lacustrine slope sediments due to seismically induced

351 subaquatic failures of lateral slopes (e.g. Schnellmann et al., 2005; Hage et al., 2017), or spontaneous slope

352 failures due to high surcharge in sediments of submerged delta slopes (e.g. Girardclos et al., 2007; Hilbe &

353 Anselmetti, 2014). The last hypothesis is less probable as slope angles are gentle in this area (less than 5°),

354 which significantly reduces the probability of such spontaneous slope failures (Schnellmann et al., 2005).

355 Turbidites are getting thinner from SW to NE (**Fig. 6**) and some of these deposits are absent in Core

356 IZN19_16, which is farther away from the closest significantly sediment contributing delta (**Fig. 3a**). The

357 frequency of these turbidites and in particular the fact that no deposit has been observed over the last 1000

358 years is difficult to explain with the "flood hypothesis". However, given the active tectonic context of the

359 region, it is plausible that such turbidites are related to shallow slope destabilizations by recurrent

360 earthquakes, as previously proposed for thin turbidites in a similar context of Lake Hazar (~ 900 km

361 southeastward on the East Anatolian Fault; Hage et al., 2017; Hubert-Ferrari et al., 2020). To evaluate this

362 potential seismic cause, the age of the turbidites, deduced from age models of cores IZN19_21 and IZN19_31

363 are compared with those of the historical earthquakes in a broader area (Ambraseys & Finkel, 1991;

364 Ambraseys & Jackson, 2000; Ambraseys, 2002; Guidoboni et al., 2005; Ambraseys, 2009; Table S1 and S2

365 in supporting information). The sensitivity of Lake Iznik to record regional earthquakes can be characterized

366 by the Earthquake-Sensitivity Threshold Index (ESTI) (Wilhelm et al., 2016), for which the sedimentation

367 rate is critical in controlling the ability of a lake system to record earthquake-induced deposits: the higher the

368 sedimentation rate is, the greater the ESTI and the more likely it is to record earthquakes. As the

369 sedimentation rate changes through time (**Fig. 7**), the ESTI of Lake Iznik might also have changed

370 accordingly. A weighting of earthquake magnitudes by the sedimentation rate over 100 years prior to the

371  event is performed, thus the relationship between the sedimentation rate and the turbidites occurrence is

372  explored in **Fig. 8.**

373  In Core IZN19_21 that spans a longer time period till 640 cal BCE, nineteen distinct event deposits are

374  observed. Six of them are older than 0 cal CE; thus predate the first historical seismicity records for this area.

375  For the thirteen remaining sandy deposits, twelve historical earthquakes can be related to turbidite deposits

376  (**Fig. 8; Table S1** in supporting information). The last event deposit, which have not been correlated with a

377  historical earthquake is identified in the higher sedimentation rate period (350 to 600 cal CE) probably related

378  to enhanced erosion by intense human activities during Roman time (Arnaud et al., 2016; Bajard et al., 2017)

379  such as agriculture as reflected in high amounts of olive-tree pollens (Miebach et al., 2016). These fields

380  were abandoned around 650 CE when Pinus pollen increased (Miebach et al., 2016). This rise in the

381  sedimentation rate explains the increased sensitivity of the lake to record ground-shaking (Wilhelm et al.,

382  2016; Rapuc et al., 2018). During such periods, the lake is prone to record earthquakes with significantly

383  smaller magnitude, which might not be reported in historical accounts. We cannot exclude that the deposit

384  could also be related to another triggering mechanism such as flood, considering that at least one flood is

385  mentioned in a historical archive for that time period during the reign of Justinian (527-565 CE) (Evans,

386  2005).

387  In Core IZN19_31, fifteen event deposits are described, all of them in the time span of historical accounts.

388  Eleven are associated with earthquakes (Table S1 in supporting information). The four others also appear in

389  the high sedimentation rate period during which the lake sensitivity was high.

390  Overall, this approach shows conclusive results as twenty-three thin turbidites can be associated with

391  earthquakes in both cores, corresponding to fourteen independent earthquakes (**Fig. 8**). Three of them

392  correspond to earthquakes recorded on the MNAF segments (29-32 CE, 121 CE, 1065 CE (**Fig. 8c, f**). In

393  turn, some historically known earthquakes such as the 368 CE or 740 CE that strongly damaged Iznik, were

394  not recorded in our sedimentary sequences. The 368 CE may be preceded by two close older events. Two

395  sandy deposits visible in Core IZN19_31 at 232 cm depth, respectively 128 cm in IZN19_21 Core (**Fig. 5**),

396  could correspond to two of the three historical earthquakes known from that time: 358, 362 and 368 CE

397  (Table S2 in supporting information). According to their distance to the lake and magnitude (**Fig. 8c, f**), 358

398  and 362 CE earthquakes, located on the NNAF at ~ 40 km from Lake Iznik (Ambraseys, 2002), are supposed

399  to be recorded as they are up to the threshold. Hence, the 358 CE earthquake, recorded in the Gulf of Izmit

400 (Çağatay et al., 2012), could have been recorded as a thick deposit (2 cm i.e. more than four times thicker

401 than all other event deposits). The overlying thinnest coarse-grained laminae could corresponds to the 362

402 CE earthquake but it was never recorded in the Marmara Sea (Çağatay et al., 2012; McHugh et al., 2014;

403 Drab et al., 2015; Yakupoğlu et al., 2019). The lack of a third deposit marking the 368 CE earthquake thus

404 likely indicates that the slopes did not have enough time to replenish the re-mobilizable sediment stock to

405 form a new turbiditic deposit within only a few years after two earlier earthquakes. Another explanation is

406 that the 362 CE has not been recorded, or its related-turbidite could have been eroded by the one of the 368

407 CE earthquake, in particularly since historical data (e.g. Guidoboni et al., 1994) indicate that Iznik was mostly

408 destroyed during the earthquake of 368 CE. Uncertainties still remain for the assignments of historical events

409 during this period, more data are needed in the lake to document this point.

410 Furthermore, Iznik was highly damaged or destroyed by other events in 29-32 CE, 740 CE and 1065 CE with

411 earthquake magnitudes estimated between 6.8 and 7.2 (Ambraseys, 2002). These magnitudes were calculated

412 from the spatial distribution of intensities around the maximum intensity zone (Ambraseys, 2002), which in

413 turn were estimated from historical accounts. Hence, variable population, changes in building vulnerability

414 over time, and exaggeration in the historical sources are difficulties affecting these estimations.

415 The 740 CE earthquake has been documented in several places within the Marmara Sea (e.g. Çağatay et al.,

416 2012; McHugh et al., 2014; Drab et al., 2015; Yakupoğlu et al., 2019), as the epicenter is supposed to be

417 located on the NNAF (Ambraseys, 2002). According to epicentral distance and to its magnitude (**Fig. 8**), it

418 should also be recorded in our sedimentary sequences. However, we could not find any evidence supporting

419 it. McHugh et al., (2014) argue that seismo-turbidite cannot be triggered far from the ruptured segment. On

420 the contrary, the 358 CE earthquake that we recorded was only recorded in the eastern part of the Izmit Gulf

421 (Çağatay et al., 2012) and not in the other Marmara Sea Basin (e.g. Yakupoğlu et al., 2019). The presumed

422 location of the 358 CE epicenter is near Izmit (Ambraseys, 2002).

423 Concerning the instrumental period, ~ 8500 earthquakes (from 1935 to 2019; **Fig. 8c, f**) occurred in an area

424 200 km around Lake Iznik and with magnitudes (reported magnitude types vary) ranging from 2.5 to 7.6

425 (USGS catalogue; https://earthquake.usgs.gov/earthquakes/search/). Among these earthquakes, only the

426 1959 CE event is close to the sensitivity threshold of the lake for Core IZN19_31, while it is below the

427 detection limit for Core IZN19_21. Near the top of the Core IZN19_31, only one turbidite is observed, which

428 could correspond to this earthquake (**Fig. 8d**). However, four recent earthquakes (1719, 1894, 1995 and 1999)

429  are not recorded in the sedimentary sequences, even though they are near the sensitivity threshold. However,

430  there are likely many more variables affecting the detection limit and a sharp threshold is not expected in

431  such a natural system (**Fig. 8f**).

432  Finally, if we consider the historical location and magnitude (Ms = 6.8) of the 1065 CE earthquake, more

433  than 20 km east of Iznik (Ambraseys, 2002), it should be below the detection limit of Lake Iznik and hence

434  should not be recorded in our cores. Furthermore, it is not recorded in the Marmara Sea (e.g. Yakupoğlu et

435  al., 2019). According to our study and the discussion below, we suggest a reconsideration of either its

436  epicenter location or its magnitude.

437  The other events (989 CE, 869 CE, 554 CE, 478 CE, 447 CE, 407 CE) have been documented in the

438  Kumburgaz Basin of the Marmara Sea, therefore they could be related to NNAF ruptures (Yakupoğlu et al.,

439  2019). The 989 CE and 478 CE are also documented in the Çınarcık Basin (Drab et al., 2015).

440  The strong correlation between historical and instrumental recordings and our sedimentary records support

441  the reliability of this conceptual approach. These results indicate that Lake Iznik's sediments record the past

442  regional seismicity on the different branches of the NAF system. Upcoming studies should take into account

443  sediment cores from different sub-basins of Lake Iznik. They will help to distinguish more accurately the

444  source(s) of such coarser grained deposits, their synchronicity in different independent locations being a

445  strong argument for their seismic trigger (e.g. Van Daele et al., 2015).

446  **5.2 Discovery of hitherto unknown subaquatic faults**

447  The bathymetric survey carried out in the lake allows to identify two subaquatic faults (**Fig. 2 and Fig. 3**).

448  The first one is located in the northern sub-basin; striking SW-NE. It is characterized by a sharp vertical scarp

449  of ~ 5 m (**Fig. 3c**), forming the northward edge of the northern sub-basin and the shoreward underwater

450  terraces (**Fig. 2a and Fig. 3c**). This fault segment runs parallel close and south to the Boyalıca Fault so that

451  we consider it is a segment of it. The terraces, with depths of 20, 40, and 45 m b.l.l., interpreted as markers

452  of past low lake levels as documented in the Gemlik Bay (Eriş et al., 2019) are offset by the fault.

453  Microseismic data document a normal slightly dextral movement on this fault during a Ms 2 earthquake

454  (Gurbuz et al., 2000) and previous seismic study described this fault as a dextral P-shear or secondary

455  synthetic shear fault (Öztürk et al., 2009). Many SW-NE faults are observed at the regional scale (**Fig. 1**),

456  suggesting they are inherited structures. The kinematic of the South Boyalıca Fault may have change thought

457    time as suggested by the left-lateral shift of the shorelines along the South Boyalıca Fault which gives a

458    peanut shape to the lake.

459    The second fault identified in Lake Iznik, previously unknown - termed Iznik Fault - strikes E-W and

460    separates the southern sub-basin from the central ridge (**Fig. 2**). The high-resolution seismic profile across

461    IFS2 shows a series of steep faults interpreted to be arranged en-echelon manner (**Fig. 4**, *Profile P3*)

462    suggesting that it presents mostly a strike-slip movement. The Iznik Fault seams to cross the entire lake; its

463    eastern prolongation joins the dextral Dırazali Fault system onshore and potentially the dextral Gemlik Fault

464    to the west (**Fig. 2**), which would suggest a right-lateral component for this fault. Besides, the smaller en-

465    echelon faults on the border between IFS2 and IFS3 is related to small depressions, which (due to the fault

466    orientation) indicate a right-lateral component. The vertical component of this fault is small as suggested by

467    its small scarp (1 m).

468    These two subaquatic faults are most likely still active as expressed by the morphological step observed on

469    the lake floor. The present activity of the Iznik Fault, in particular, is indicated by the change in sedimentation

470    rate across the structure and the occurrence of many pock marks indicating fluid escape along the fault. Such

471    fluid venting likely indicates by deep-seated pathways along the buried fault plane (**Fig. 3b**).

472        **5.3 Identification of the last earthquake rupture on the Iznik Fault**

473    The core-to-core correlation across the Iznik Fault (IFS1 on **Fig. 3a**) allows to identify thicknesses variations

474    of sedimentary units across the structure. For the present-day profile (**Fig. 9a**), the topography is deduced

475    from the multibeam bathymetry (Profile P1 on **Fig. 3a**). From the sediment-core analysis we retrieved the

476    paleotopography and sedimentological features at different moments by removing unit by unit from the top

477    to the bottom of the cores. For each depth, the age is determined from the age models of cores IZN19_21 and

478    IZN19_31 (**Fig. 7**); the total uncertainty range of the different ages allows to encompass the time span. After

479    removing the pink and green units (**Fig. 9b**), the residual topography is assumed to be the paleo topography

480    at 1000/1154 cal CE. Compaction and erosion are neglected on this reconstruction, as we suppose a similar

481    effect on both sides of the fault as well as similar erosional processes (e.g. deep currents). This reconstruction

482    highlights a sediment thickness variation of ~ 40 cm between the hanging and the footwall of the fault for

483    the green unit as opposed to only a minor relative difference in thickness for the orange unit just below (**Fig.**

484    **9**). This thickness variation reflects the fault activity. The co-seismic vertical offset created an

485    accommodation space on the footwall of the fault which then has been gradually filled (**Fig. 9b**). Part of this

486 thickness variation on both side of the fault can also be due to the dextral co-seismic offset that bring finer

487 sediments on the northern compartment of the fault compare to more proximal and thicker ones in the

488 southern compartment. The observation of an event deposit at the base of this green unit also supports this

489 interpretation of fault rupture (**Fig. 8a**). The turbidity current-induced deposit is a co-seismic marker while

490 the sedimentary thickness variation is a syn- to post-seismic indicator. This co-seismic event deposit is dated

491 between 1000 to 1154 cal. CE and thus coincides with the well-documented 1065 CE earthquake (Ambraseys,

492 2009). The independent archeo-seismological study of Benjelloun et al., (2020), documents an important

493 phase of reconstruction of Nicaea's buildings (formerly Iznik) between 858 and 1097 CE. According to the

494 original historical archive (Michael & Attaleiatēs, 2012), the 1065 CE earthquake has strongly damaged the

495 city of Iznik (formerly Nicaea/ Nikaia): "It happened at Nikaia in Bithynia and brought almost total

496 devastation and ruin to the place. Its most important and large churches [...] and the one of the Holy Fathers,

497 where the Council of the most Holy and Orthodox Fathers against Areios confirmed its decisions [...] those

498 churches, then, were shaken and collapsed as did the walls of the city along with many private dwellings.".

499 No other locality seems to have been damaged as strongly as Iznik during this earthquake, which suggests a

500 proximal event rupturing the MNAF. The ~ 40 cm vertical co-seismic offset associated to the dextral one and

501 the co-seismic turbidites could have triggered a destructive wave (tsunami). This 1065 CE earthquake may

502 have also induced ground-level variation that led to the destruction and submersion of the basilica of Nicaea

503 (Şahin, 2014), explaining why this basilica has never been rebuilt.

504 As shown in **Fig. 8**, the 1065 CE earthquake should not be recorded in our cores if we consider the epicenter

505 location deduced from historical archives >20 km east of Iznik (Ambraseys, 2002) and it has not been

506 documented neither in other lake (e.g. Sapanca) nor in the Marmara Sea basins (e.g. Yakupoğlu et al., 2019).

507 However, we show in this study that both an event deposit and a sedimentary unit with a vertical offset by ~

508 40 cm are dated to that period. As this earthquake clearly ruptured the Iznik Fault up to the lake floor we

509 propose to relocate the position of its epicenter in the lake (black arrow on **Fig. 8**). As McHugh et al., (2014)

510 reported, the location of historical earthquakes can present big errors since the fault segments within the

511 Marmara Sea and the different lakes were not known before the 1999 CE Izmit Earthquake.

512 The most recent unit (pink in **Fig. 9a**) postdates 1470/1777 cal. CE and shows a thickness increase of ~ 44

513 cm in the southernmost shore-proximal Core IZN19_04. Bathymetric data suggest a recent delta-derived

514   clastic contribution to explain this thickness variation. The recent increase of erosion and sediment supply to

515   the lake is likely related to agriculture revival in the catchment (Geyer et al., 2001).

516   The lowermost stratigraphic unit found in our cores, the unit marked in grey, is 62 cm thicker on the southern

517   side of the fault (62 cm vs. <130 cm) (**Fig. 9c**). Such a variation could be also caused by movements of the

518   fault during former earthquakes before the common era, suggesting thousand years of recurrence on this fault

519   segment. But longer sequences are required on both side of the fault to retrieved the base of the grey unit and

520   infer the pre-grey unit topography to confirm this hypothesis. Further seismic acquisitions could also help to

521   highlight and image stratigraphically deeper units in the hanging wall (e.g. Beck et al., 2012), and to identify

522   the horizontal offset along the fault. The core locations are ideal to identify the rupture on the Iznik Fault,

523   but cores in the deepest sub-basins could be more prone to record and earthquake catalogue (e.g. McHugh et

524   al., 2014).

525            **5.4 Regional tectonics**

526   Looking at a larger scale, the identification of an earthquake rupture on the Iznik Fault in 1065 CE is of major

527   importance as it belongs to the MNAF system. According to the synthesis of Drab et al., (2015), a sequence

528   of earthquakes is observed from 865 to 1063 along the NNAF, with a seismic gap within the central Marmara

529   Sea, quite similar as the one we observed presently. The 1065 CE earthquake that occurs on the MNAF

530   accommodates part of the accumulated stress at the NAF scale, showing the complexity of this system of

531   faults. The fact that this Iznik Fault has not ruptured since almost thousand years (last rupture in 1065 CE)

532   and that a gap of seismicity is observed all along the MNAF, the seismic hazard increases a lot in this area.

533   Linear strike-slip faults such as the Iznik Fault are important tectonic structures as shown by the one

534   discovered along the NNAF within the Izmit-Sapanca segment during the Izmit 1999 earthquake (Michel &

535   Avouac, 2002). The rupture along this straight segment was of supershear nature and caused strong damages

536   amplified by ground liquefaction (Bouchon, 2002). The presented newly discovered faults provide essential

537   data showing that the MNAF should be seriously consider in the assessment of seismic hazard of the region.

538   The description of the whole active fault system in and around Lake Iznik also improves tectonic knowledge.

539   The Gürle and Orhangazi normal faults bounded the underwater Iznik and South Boyalıca faults, resulting in

540   a negative flower structure linked to the MNAF system, as shown on the simplified NS cross section of the

541   lake (Demirel et al., 2020; **Fig. 10b**). Lake Iznik exhibits three sub-basins that cannot be explained in a simple

542   pull-apart process approach (Wu et al., 2009; Dooley & Schreurs, 2012). The South Boyalıca Fault presented

543    in this study seems to delimit the western sub-basin from the two others (**Fig. 10a**), when the Iznik Fault

544    delineates the southern basin. Models of transtensional pull-apart basins, due to an oblique and divergent

545    displacement at a θ angle with the main strike-slip fault show similar sub-basins delineated by faults (Wu et

546    al., 2009; Dooley & Schreurs, 2012; **Fig. 10a**). This hypothesis of transtension is supported by the GPS data

547    along the MNAF in this area (Akay & Ozener, 2009).

548    The discovery of the Iznik strike-slip Fault also suggests fault partitioning of the MNAF close to Lake Iznik.

549    The onshore Gürle Fault accommodates mostly the normal component and controls the deepest basin of the

550    lake whereas the Iznik Fault accommodates the right-lateral component of the MNAF system, controlling the

551    shape of the southern sub-basin (**Fig. 10**). Two smaller N-S extensional fault segments were observed on the

552    western sub-basin (Öztürk et al., 2009) and to the East of the city of Iznik (the Ebeyli Fault) (Benjelloun et

553    al., 2018). Scarps with similar strike are observed in the bathymetric map from the DSI that need to be studied

554    more closely (**Fig. 10a**). Further bathymetric and seismic surveys will provide key elements to understand

555    the timing of these tectonic controls. Airgun seismic data could also provide more information on the fault

556    activities over time and image the subsurface continuation of the fault (e.g. de La Taille et al., 2015).

557    ## 6.  Conclusions

558    The sedimentary study done on the cores sampled in the Lake Iznik revealed fourteen earthquake-induced

559    turbidite deposits since their ages correspond to historical regional seismic events during the past two

560    millennia, allowing to refine the calendar of historical seismicity in this region (29-32, 69, 121, 269, 358, 362

561    or 368, 407, 447, 478, 554, 869, 989, 1065, 1959 CE). At least three of them are related to the MNAF rupture

562    (32, 121, 1065 CE).

563    The combined geophysical and sedimentological approach in Lake Iznik allows to discover two active

564    subaquatic faults, the South Boyalıca and Iznik faults, that form part of the middle strand of the North

565    Anatolian Fault system and that are responsible for some of the recorded earthquakes in the lake. The

566    sedimentological study focused on both part of the Iznik Fault shows paleo-seismological evidences for a

567    last rupture that occurred during the devastating 1065 CE earthquake. Longer sequences from the same

568    locations associated to on-fault studies are needed to determine the earthquake recurrence interval on the

569    Iznik Fault which seems to be close to 1000 years. The seismic gap since 1065 CE of this Iznik Fault segment

570    strongly increases the seismic hazard in the region of Iznik and must be taken into account for the seismic

571    risk assessment of the NAF system. At the scale of the NAF system the 1065 CE earthquake could belongs

572    to the sequence of earthquakes from 865 CE to 1065 CE, when a seismic gap was subsisting along the NNAF

573    within the central Marmara Sea, showing that the MNAF takes an active part in the seismic cycle of the NAF.

574    Finally, our findings provide a better understanding of the Lake Iznik tectonic context that presents a negative

575    flower structure with a transtensional component.

## Data availability

591    Supplementary data reported in this study are given in the supporting information, and all core and

592    geophysical data are stored in Pangaea database (at https://doi.org/10.1594/PANGAEA.924472,

593    https://doi.org/10.1594/PANGAEA.924476,    https://doi.org/10.1594/PANGAEA.924477,

594    https://doi.org/10.1594/PANGAEA.924479,    https://doi.org/10.1594/PANGAEA.924482,

595    https://doi.org/10.1594/PANGAEA.924483,    https://doi.org/10.1594/PANGAEA.924489,

596    https://doi.org/10.1594/PANGAEA.924492,    https://doi.org/10.1594/PANGAEA.924495,

597    https://doi.org/10.1594/PANGAEA.924496, and https://doi.org/10.1594/PANGAEA.924497).

598

599

## Author contributions

RG performed the analysis and wrote the main manuscript file and figures. JS designed the research project. PS dynamically assisted throughout the whole research process, during all stages of analysis and interpretations of the cores. SF and FA led the bathymetric campaign and assisted the geophysical data processing. RG, JS, SF, FA, SG sampled the cores. ALD assisted acquisition and interpretation of XRF analysis. MŞ and SG provided invaluable assistance during the different field campaigns. CG and FN provided the seismic data from a previous field campaign. JS, PS, SF, FA and CG actively corrected and improved the manuscript. Each author has proofread and corrected the manuscript at least once.

## References

Akay, G., & Ozener, H. (2009). Investigation of long period crustal deformation on the inactive branch of the North Anatolian Fault Zone. *Natural Hazards and Earth System Sciences*, *9*(3), 663–671. https://doi.org/10.5194/nhess-9-663-2009

Ambraseys. (2002). The Seismic Activity of the Marmara Sea Region over the Last 2000 Years. *Bulletin of the Seismological Society of America*, *92*(1), 1–18. https://doi.org/10.1785/0120000843

Ambraseys. (2009). *Earthquakes in the Mediterranean and Middle East: a multidisciplinary study of seismicity up to 1900*. Cambridge University Press.

Ambraseys, & Finkel, C. (1991). Long-term seismicity of Istanbul and of the Marmara Sea region. *Terra Nova*, *3*(5), 527–539.

Ambraseys, N. N., & Jackson, J. A. (2000). Seismicity of the Sea of Marmara (Turkey) since 1500. *Geophysical Journal International*, *141*(3), F1–F6. https://doi.org/10.1046/j.1365-246x.2000.00137.x

Armijo, R., Pondard, N., Meyer, B., Uçarkus, G., de Lépinay, B. M., Malavieille, J., et al. (2005). Submarine fault scarps in the Sea of Marmara pull-apart (North Anatolian Fault): Implications for seismic hazard in Istanbul. *Geochemistry, Geophysics, Geosystems*, *6*(6).

Arnaud, F., Poulenard, J., Giguet-Covex, C., Wilhelm, B., Révillon, S., Jenny, J.-P., et al. (2016). Erosion under climate and human pressures: An alpine lake sediment perspective. *Quaternary Science Reviews*, *152*, 1–18. https://doi.org/10.1016/j.quascirev.2016.09.018

Avşar, U., Hubert-Ferrari, A., De Batist, M., Schmidt, S., & Fagel, N. (2015). Sedimentary records of past earthquakes in Boraboy Lake during the last ca 600 years (North Anatolian Fault, Turkey).

629     *Palaeogeography,       Palaeoclimatology,       Palaeoecology*,       *433*,       1–9.

630          https://doi.org/10.1016/j.palaeo.2015.04.031

631     Bajard, M., Poulenard, J., Sabatier, P., Develle, A.-L., Giguet-Covex, C., Jacob, J., et al. (2017). Progressive

632          and   regressive   soil   evolution   phases   in   the   Anthropocene.   *CATENA*,   *150*,   39–52.

633          https://doi.org/10.1016/j.catena.2016.11.001

634     Barka, A. (1993). Kuzey Anadolu Fayının Sapanca-İzmit ve Geyve-İznik kolları üzerinde paleosismik

635          araştırmalar. *TÜBİTAK Proje No: YBAG-4/7551*, 85.

636     Beck, C., Reyss, J.-L., Leclerc, F., Moreno, E., Feuillet, N., Barrier, L., et al. (2012). Identification of deep

637          subaqueous co-seismic scarps through specific coeval sedimentation in Lesser Antilles: implication

638          for   seismic   hazard.   *Natural   Hazards   and   Earth   System   Sciences*,   *12*(5),   1755–1767.

639          https://doi.org/10.5194/nhess-12-1755-2012

640     Beck, C., Campos, C., Eriş, K. K., Çağatay, N., Mercier de Lepinay, B., & Jouanne, F. (2015). Estimation of

641          successive coseismic vertical offsets using coeval sedimentary events &amp;ndash; application to

642          the southwestern limit of the Sea of Marmara's Central Basin (North Anatolian Fault). *Natural*

643          *Hazards and Earth System Sciences*, *15*(2), 247–259. https://doi.org/10.5194/nhess-15-247-2015

644     Beck, Christian. (2009). Late Quaternary lacustrine paleo-seismic archives in north-western Alps: Examples

645          of earthquake-origin assessment of sedimentary disturbances. *Earth-Science Reviews*, *96*(4), 327–

646          344.

647     Benjelloun, Y. (2017). *The middle strand of the North Anatolian fault in Iznik region : insights from*

648          *geomorphology   and   archeoseismology*   (Doctoral   dissertation).   Université   Grenoble   Alpes.

649          Retrieved from https://tel.archives-ouvertes.fr/tel-01952234

650     Benjelloun, Y., De Sigoyer, J., Dessales, H., Baillet, L., Guéguen, P., & Şahin, M. (2020). Historical

651          earthquake scenarios for the middle strand of the North Anatolian Fault deduced from archeo-

652          damage inventory and building deformation modeling. *Seismological Research Letters*.

653     Benjelloun, Yacine, de Sigoyer, J., Dessales, H., Garambois, S., & Şahin, M. (2018). Construction history of

654          the aqueduct of Nicaea (Iznik, NW Turkey) and its on-fault deformation viewed from archaeological

655          and   geophysical   investigations.   *Journal   of   Archaeological   Science:   Reports*,   *21*,   389–400.

656          https://doi.org/10.1016/j.jasrep.2018.08.010

657    Blaauw, M. (2010). Methods and code for 'classical'age-modelling of radiocarbon sequences. *Quaternary*

658         *Geochronology*, *5*(5), 512–518.

659    Bouchon, M. (2002). Space and Time Evolution of Rupture and Faulting during the 1999 Izmit (Turkey)

660         Earthquake. *Bulletin of the Seismological Society of America*, *92*(1), 256–266.

661         https://doi.org/10.1785/0120000845

662    Brocard, G., Anselmetti, F. S., & Teyssier, C. (2016). Guatemala paleoseismicity: from Late Classic Maya

663         collapse to recent fault creep. *Scientific Reports*, *6*, 36976.

664    Bulut, F., Aktuğ, B., Yaltırak, C., Doğru, A., & Özener, H. (2019). Magnitudes of future large earthquakes

665         near Istanbul quantified from 1500 years of historical earthquakes, present-day microseismicity and

666         GPS slip rates. *Tectonophysics*, *764*, 77–87.

667    Çağatay, M., Erel, L., Bellucci, L., Polonia, A., Gasperini, L., Eriş, K., et al. (2012). Sedimentary earthquake

668         records in the İzmit gulf, sea of Marmara, Turkey. *Sedimentary Geology*, *282*, 347–359.

669    Cetin, K. O., Youd, T. L., Seed, R. B., Bray, J. D., Sancio, R., Lettis, W., et al. (2002). Liquefaction-induced

670         ground deformations at Hotel Sapanca during Kocaeli (Izmit),Turkey earthquake. *Soil Dynamics*

671         *and Earthquake Engineering*, *22*(9–12), 1083–1092. https://doi.org/10.1016/S0267-

672         7261(02)00134-3

673    Cukur, D., Krastel, S., Demirel-Schlüter, F., Demirbağ, E., Imren, C., Niessen, F., et al. (2013). Sedimentary

674         evolution of Lake Van (Eastern Turkey) reconstructed from high-resolution seismic investigations.

675         *International Journal of Earth Sciences*, *102*(2), 571–585. https://doi.org/10.1007/s00531-012-

676         0816-x

677    Demirel, S., Alpar, B., Yaltırak, C., Vardar, D., & Kurt, H. (2020). Northern segment of the North Anatolian

678         Fault in the Gulf of Izmit inferred from marine magnetic anomalies. *Marine Geophysical Research*,

679         *41*(1), 6. https://doi.org/10.1007/s11001-020-09399-6

680    Doğan, B. (2010). *Kuzey Anadolu Fay Sistemi Güney Kolunun Geyve-gemlik Arasındaki Kesiminin*

681         *Morfotektonik, Tektonostratigrafik Ve Paleosismolojik Evrimi* (PhD Thesis). Fen Bilimleri

682         Enstitüsü.

683    Doğan, B., Tüysüz, O., & Şanlı, F. B. (2015). Tectonostratigraphic evolution of the basins on the southern

684         branch of the North Anatolian Fault System in the SE Marmara Region, Turkey. *International*

685         *Journal of Earth Sciences*, *104*(2), 389–418. https://doi.org/10.1007/s00531-014-1083-9

686    Dooley, T. P., & Schreurs, G. (2012). Analogue modelling of intraplate strike-slip tectonics: A review and

687        new experimental results. *Tectonophysics*, *574*, 1–71.

688    Drab, L., Hubert, A., Schmidt, S., & Martinez, P. (2012). The earthquake sedimentary record in the western

689        part of the Sea of Marmara, Turkey. *Natural Hazards and Earth System Sciences*.

690    Drab, L., Hubert-Ferrari, A., Schmidt, S., Martinez, P., Carlut, J., & Ouahabi, M. E. (2015). Submarine

691        Earthquake History of the Çınarcık Segment of the North Anatolian Fault in the Marmara Sea,

692        TurkeySubmarine Earthquake History of the Çınarcık Segment of the NAF in the Marmara Sea,

693        Turkey. *Bulletin of the Seismological Society of America*, *105*(2A), 622–645.

694        https://doi.org/10.1785/0120130083

695    EarthExplorer - Home. (n.d.). Retrieved June 15, 2020, from https://earthexplorer.usgs.gov/

696    Emre, Ö., Duman, T. Y., Özalp, S., Şaroğlu, F., Olgun, Ş., Elmacı, H., & Çan, T. (2018). Active fault database

697        of Turkey. *Bulletin of Earthquake Engineering*, *16*(8), 3229–3275. https://doi.org/10.1007/s10518-

698        016-0041-2

699    Ergintav, S., Reilinger, R., Çakmak, R., Floyd, M., Cakir, Z., Doğan, U., et al. (2014). Istanbul's earthquake

700        hot spots: Geodetic constraints on strain accumulation along faults in the Marmara seismic gap.

701        *Geophysical Research Letters*, *41*(16), 5783–5788.

702    Eriş, K Kadir, Çağatay, N., Beck, C., de Lepinay, B. M., & Corina, C. (2012). Late-Pleistocene to Holocene

703        sedimentary fills of the Çınarcık Basin of the Sea of Marmara. *Sedimentary Geology*, *281*, 151–165.

704    Eriş, Kürşad Kadir, Sabuncu, A., Gasperini, L., Polonia, A., & Kındap, T. (2019). Influence of climate on

705        the late Pleistocene depositional history of the Gulf of Gemlik (Sea of Marmara). *Geo-Marine*

706        *Letters*, *39*(3), 205–221.

707    Evans, J. A. S. (2005). *The Emperor Justinian and the Byzantine Empire*. Greenwood Publishing Group.

708    Geyer, martin, & al. (2001). *Castrum 7: Zones côtières littorales dans le monde Méditerranéen au Moyen*

709        *Âge : défense, peuplement, mise en valeur*. Casa de Velázquez.

710    Girardclos, S., Schmidt, O. T., Sturm, M., Ariztegui, D., Pugin, A., & Anselmetti, F. S. (2007). The 1996 AD

711        delta collapse and large turbidite in Lake Brienz. *Marine Geology*, *241*(1–4), 137–154.

712    Guevara, S. R., Rizzo, A., Daga, R., Williams, N., & Villa, S. (2019). Bromine as indicator of source of

713        lacustrine sedimentary organic matter in paleolimnological studies. *Quaternary Research*, *92*(1),

714        257–271.

715 Guidoboni, E., Comastri, A., Traina, G., & Geofisica, R. I. N. di. (1994). *Catalogue of Ancient Earthquakes*
716       *in the Mediterranean Area up to the 10th Century*. Istituto nazionale di geofisica Rome.

717 Guidoboni, E., Comastri, A., Storia, S., & others. (2005). *Catalogue of Earthquakes and Tsunamis in the*
718       *Mediterranean Area from the 11th to the 15th Century*.

719 Gurbuz, C., Aktar, M., Eyidogan, H., Cisternas, A., Haessler, H., Barka, A., et al. (2000). The seismotectonics
720       of the Marmara region (Turkey): results from a microseismic experiment. *Tectonophysics*, *316*(1),
721       1–17. https://doi.org/10.1016/S0040-1951(99)00253-X

722 Hage, S., Hubert-Ferrari, A., Lamair, L., Avşar, U., El Ouahabi, M., Van Daele, M., et al. (2017). Flow
723       dynamics at the origin of thin clayey sand lacustrine turbidites: Examples from Lake Hazar, Turkey.
724       *Sedimentology*, *64*(7), 1929–1956. https://doi.org/10.1111/sed.12380

725 Heiri, O., Lotter, A. F., & Lemcke, G. (2001). Loss on ignition as a method for estimating organic and
726       carbonate content in sediments: reproducibility and comparability of results. *Journal of*
727       *Paleolimnology*, *25*(1), 101–110.

728 Hilbe, M., & Anselmetti, F. S. (2014). Signatures of slope failures and river-delta collapses in a perialpine
729       lake (Lake Lucerne, Switzerland). *Sedimentology*, *61*(7), 1883–1907.
730       https://doi.org/10.1111/sed.12120

731 Honkura, Y., & Işikara, A. M. (1991). Multidisciplinary research on fault activity in the western part of the
732       North Anatolian Fault Zone. *Tectonophysics*, *193*(4), 347–357. https://doi.org/10.1016/0040-
733       1951(91)90343-Q

734 Hubert-Ferrari, A., Barka, A., Jacques, E., Nalbant, S. S., Meyer, B., Armijo, R., et al. (2000). Seismic hazard
735       in the Marmara Sea region following the 17 August 1999 Izmit earthquake. *Nature*, *404*(6775), 269–
736       273. https://doi.org/10.1038/35005054

737 Hubert-Ferrari, A., Lamair, L., Hage, S., Schmidt, S., Çağatay, M. N., & Avşar, U. (2020). A 3800 yr
738       paleoseismic record (Lake Hazar sediments, eastern Turkey): Implications for the East Anatolian
739       Fault seismic cycle. *Earth and Planetary Science Letters*, *538*, 116152.

740 Kurt, H., Sorlien, C., Seeber, L., Steckler, M., Shillington, D., Cifci, G., et al. (2013). Steady late quaternary
741       slip rate on the Cinarcik section of the North Anatolian fault near Istanbul, Turkey. *Geophysical*
742       *Research Letters*, *40*(17), 4555–4559.

743 de La Taille, C., Jouanne, F., Crouzet, C., Beck, C., Jomard, H., de Rycker, K., & Van Daele, M. (2015).

744 Impact of active faulting on the post LGM infill of Le Bourget Lake (western Alps, France).

745 *Tectonophysics*, *664*, 31–49. https://doi.org/10.1016/j.tecto.2015.08.024

746 Lange, D., Kopp, H., Royer, J.-Y., Henry, P., Çakir, Z., Petersen, F., et al. (2019). Interseismic strain build-

747 up on the submarine North Anatolian Fault offshore Istanbul. *Nature Communications*, *10*(1), 1–9.

748 McHugh, C. M., Seeber, L., Cormier, M.-H., Dutton, J., Cagatay, N., Polonia, A., et al. (2006). Submarine

749 earthquake geology along the North Anatolia Fault in the Marmara Sea, Turkey: A model for

750 transform basin sedimentation. *Earth and Planetary Science Letters*, *248*(3–4), 661–684.

751 McHugh, C. M. G., Braudy, N., Çağatay, M. N., Sorlien, C., Cormier, M.-H., Seeber, L., & Henry, P. (2014).

752 Seafloor fault ruptures along the North Anatolia Fault in the Marmara Sea, Turkey: Link with the

753 adjacent basin turbidite record. *Marine Geology*, *353*, 65–83.

754 https://doi.org/10.1016/j.margeo.2014.03.005

755 Michael, A., & Attaleiatēs, M. (2012). *The History* (Vol. 16). Harvard University Press.

756 Michel, R., & Avouac, J.-P. (2002). Deformation due to the 17 August 1999 Izmit, Turkey, earthquake

757 measured from SPOT images. *Journal of Geophysical Research: Solid Earth*, *107*(B4), ETG 2-1-

758 ETG 2-6. https://doi.org/10.1029/2000JB000102

759 Miebach, A., Niestrath, P., Roeser, P., & Litt, T. (2016). Impacts of climate and humans on the vegetation in

760 northwestern Turkey: palynological insights from Lake Iznik since the Last Glacial. *Climate of the*

761 *Past*, *12*(2), 575–593. https://doi.org/10.5194/cp-12-575-2016

762 Moernaut, J., Van Daele, M., Strasser, M., Clare, M. A., Heirman, K., Viel, M., et al. (2017). Lacustrine

763 turbidites produced by surficial slope sediment remobilization: A mechanism for continuous and

764 sensitive turbidite paleoseismic records. *Marine Geology*, *384*, 159–176.

765 https://doi.org/10.1016/j.margeo.2015.10.009

766 Monecke, K., Anselmetti, F. S., Becker, A., Sturm, M., & Giardini, D. (2004). The record of historic

767 earthquakes in lake sediments of Central Switzerland. *Tectonophysics*, *394*(1–2), 21–40.

768 Munsell Color. (1994). *Munsell Soil Color Charts. Macbeth, Division of Kollmorgen Instruments*

769 *Corporation*. Newburgh, NY: Munsell Color.

770 Öcal, A. (2019). Natural Disasters in Turkey: Social and Economic Perspective. *International Journal of*

771 *Disaster Risk Management*, *1*(1), 51–61.

772 Özalp, S., Emre, Ö., & Dogan, A. (2013). The segment structure of southern branch of the North Anatolian

773         Fault and paleoseismological behaviour of the Gemlik Fault, NW Anatolia. *General Directorate of*

774         *Mineral Research and Exploration (MTA) Bulletin*, *147, 1–17.*

775 Öztürk, K., Yaltirak, C., & Alpar, B. (2009). The relationship between the tectonic setting of the Lake Iznik

776         basin and the middle strand of the North Anatolian Fault. *Turkish Journal of Earth Sciences*, *18*(2),

777         209–224.

778 Parsons, T. (2000). Heightened Odds of Large Earthquakes Near Istanbul: An Interaction-Based Probability

779         Calculation. *Science*, *288*(5466), 661–665. https://doi.org/10.1126/science.288.5466.661

780 R Core Team. (2018). *R: A Language and Environment for Statistical Computing*. Vienna, Austria: R

781         Foundation for Statistical Computing. Retrieved from https://www.R-project.org/

782 Rapuc, W., Sabatier, P., Andrič, M., Crouzet, C., Arnaud, F., Chapron, E., et al. (2018). 6600 years of

783         earthquake record in the Julian Alps (Lake Bohinj, Slovenia). *Sedimentology*, *65*(5), 1777–1799.

784         https://doi.org/10.1111/sed.12446

785 Reilinger, R., McClusky, S., Vernant, P., Lawrence, S., Ergintav, S., Cakmak, R., et al. (2006). GPS

786         constraints on continental deformation in the Africa-Arabia-Eurasia continental collision zone and

787         implications for the dynamics of plate interactions. *Journal of Geophysical Research: Solid Earth*,

788         *111*(B5).

789 Reimer, P. J., Austin, W. E., Bard, E., Bayliss, A., Blackwell, P. G., Ramsey, C. B., et al. (2020). The IntCal20

790         Northern Hemisphere radiocarbon age calibration curve (0–55 cal kBP). *Radiocarbon*, 1–33.

791 Richter, T. O., Van der Gaast, S., Koster, B., Vaars, A., Gieles, R., de Stigter, H. C., et al. (2006). The

792         Avaatech XRF Core Scanner: technical description and applications to NE Atlantic sediments.

793         *Geological Society, London, Special Publications*, *267*(1), 39–50.

794 Roeser, P., Franz, S. O., & Litt, T. (2016). Aragonite and calcite preservation in sediments from Lake Iznik

795         related to bottom lake oxygenation and water column depth. *Sedimentology*, *63*(7), 2253–2277.

796         https://doi.org/10.1111/sed.12306

797 Roeser, P. A. (2014). *Paleolimnology of Lake Iznik (NW Turkey) during the past ~ 31 ka cal BP*.

798 Roeser, P. A., Franz, S. O., Litt, T., Ülgen, U. B., Hilgers, A., Wulf, S., et al. (2012). Lithostratigraphic and

799         geochronological framework for the paleoenvironmental reconstruction of the last ~36 ka cal BP

800      from a sediment record from Lake Iznik (NW Turkey). *Quatenary International*, *274*, 73–87.

801      https://doi.org/10.1016/j.quaint.2012.06.006

802  Roodenberg, J. (2013). Change in food production and its impact on an early 6th millennium community in

803      northwest Anatolia. The example of Ilıpınar. *Praehistorische Zeitschrift*, *87*(2), 223–235.

804  Sabatier, P., Dezileau, L., Briqueu, L., Colin, C., & Siani, G. (2010). Clay minerals and geochemistry record

805      from northwest Mediterranean coastal lagoon sequence: Implications for paleostorm reconstruction.

806      *Sedimentary Geology*, *228*(3–4), 205–217.

807  Şahin, M. (2014). İznik Gölü'ndeki Batık Kilise: Deprem Kurbanı Aziz Neophytos. *Aktüel Arkeoloji 38*,

808      *Nisan, 8-10.*

809  Şahin, M., & R. Fairchild, M. (2018). Nicea's Underwater Basilica. *Biblical Archaeology*, *Review 44:6.*

810  Schnellmann, M., Anselmetti, F. S., Giardini, D., & McKENZIE, J. A. (2005). Mass movement-induced fold-

811      and-thrust belt structures in unconsolidated sediments in Lake Lucerne (Switzerland).

812      *Sedimentology*, *52*(2), 271–289.

813  Şengör, A., Grall, C., İmren, C., Le Pichon, X., Görür, N., Henry, P., et al. (2014). The geometry of the North

814      Anatolian transform fault in the Sea of Marmara and its temporal evolution: implications for the

815      development of intracontinental transform faults. *Canadian Journal of Earth Sciences*, *51*(3), 222–

816      242.

817  Stein, R. S., Barka, A. A., & Dieterich, J. H. (1997). Progressive failure on the North Anatolian fault since

818      1939 by earthquake stress triggering. *Geophysical Journal International*, *128*(3), 594–604.

819      https://doi.org/10.1111/j.1365-246X.1997.tb05321.x

820  Strasser, M., Anselmetti, F. S., Fäh, D., Giardini, D., & Schnellmann, M. (2006). Magnitudes and source

821      areas of large prehistoric northern Alpine earthquakes revealed by slope failures in lakes. *Geology*,

822      *34*(12), 1005. https://doi.org/10.1130/G22784A.1

823  Strasser, M., Monecke, K., Schnellmann, M., & Anselmetti, F. S. (2013). Lake sediments as natural

824      seismographs: A compiled record of Late Quaternary earthquakes in Central Switzerland and its

825      implication for Alpine deformation. *Sedimentology*, *60*(1), 319–341.

826      https://doi.org/10.1111/sed.12003

827  Tibi, R., Bock, G., Xia, Y., Baumbach, M., Grosser, H., Milkereit, C., et al. (2001). Rupture processes of the

828     1999 August 17 Izmit and November 12 Düzce (Turkey) earthquakes. *Geophysical Journal*

829     *International*, *144*(2), F1–F7.

830  Uçarkuş, G. (2002). *Gemlik Fay Zonu'nun Aktif Tektoniği* (Doctoral dissertation). İstanbul Teknik

831     Üniversitesi.

832  Ülgen, U. B., Franz, S. O., Biltekin, D., Çagatay, M. N., Roeser, P. A., Doner, L., & Thein, J. (2012). Climatic

833     and environmental evolution of Lake Iznik (NW Turkey) over the last ∼4700 years. *Quaternary*

834     *International*, *274*, 88–101. https://doi.org/10.1016/j.quaint.2012.06.016

835  Van Daele, M., Moernaut, J., Doom, L., Boes, E., Fontijn, K., Heirman, K., et al. (2015). A comparison of

836     the sedimentary records of the 1960 and 2010 great Chilean earthquakes in 17 lakes: Implications

837     for quantitative lacustrine palaeoseismology. *Sedimentology*, *62*(5), 1466–1496.

838     https://doi.org/10.1111/sed.12193

839  Viehberg, F. A., Ülgen, U. B., Damcı, E., Franz, S. O., Ön, S. A., Roeser, P. A., et al. (2012). Seasonal

840     hydrochemical changes and spatial sedimentological variations in Lake Iznik (NW Turkey).

841     *Quaternary International*, *274*, 102–111. https://doi.org/10.1016/j.quaint.2012.05.038

842  Wilhelm, B., Sabatier, P., & Arnaud, F. (2015). Is a regional flood signal reproducible from lake sediments?

843     *Sedimentology*, *62*(4), 1103–1117. https://doi.org/10.1111/sed.12180

844  Wilhelm, B., Nomade, J., Crouzet, C., Litty, C., Sabatier, P., Belle, S., et al. (2016). Quantified sensitivity of

845     small lake sediments to record historic earthquakes: Implications for paleoseismology: LAKE

846     SENSITIVITY TO RECORD EARTHQUAKES. *Journal of Geophysical Research: Earth Surface*,

847     *121*(1), 2–16. https://doi.org/10.1002/2015JF003644

848  Wu, J. E., McClay, K., Whitehouse, P., & Dooley, T. (2009). 4D analogue modelling of transtensional pull-

849     apart basins. *Marine and Petroleum Geology*, *26*(8), 1608–1623.

850     https://doi.org/10.1016/j.marpetgeo.2008.06.007

851  Yakupoğlu, N., Uçarkuş, G., Eriş, K. K., Henry, P., & Çağatay, M. N. (2019). Sedimentological and

852     geochemical evidence for seismoturbidite generation in the Kumburgaz Basin, Sea of Marmara:

853     Implications for earthquake recurrence along the Central High Segment of the North Anatolian Fault.

854     *Sedimentary Geology*, *380*, 31–44.

855    Yaltırak, C. (2002). Tectonic evolution of the Marmara Sea and its surroundings. *Marine Geology*, *190*(1–

856          2), 493–529. https://doi.org/10.1016/S0025-3227(02)00360-2

857

858

859
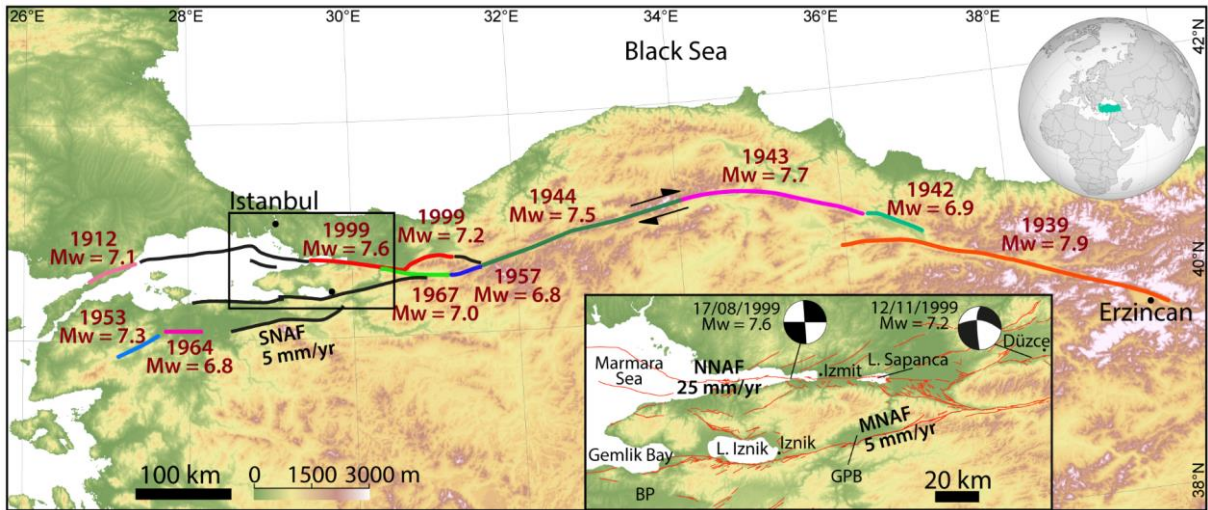
**Fig. 1**: Shuttle Radar Topography Mission (SRTM - 1 arc-second resolution; https://earthexplorer.usgs.gov/) digital elevation model (DEM) with the different fault strands that ruptured during the major earthquakes of the 20th century (respective age, location and moment magnitudes indicated from USGS earthquake catalog; https://earthquake.usgs.gov/earthquakes/search/ and Stein et al., (1997)). The seismic gaps at the western termination of the NAF are shown as black lines. Inset is a zoom of the studied part with the different strands of the NAF. GPB refers to the Geyve-Pamukova Basin, BP to the Bursa Province. Focal mechanism solutions are retrieved from Tibi et al., (2001). Active faults are shown in red (Benjelloun, 2017; Emre et al., 2018).
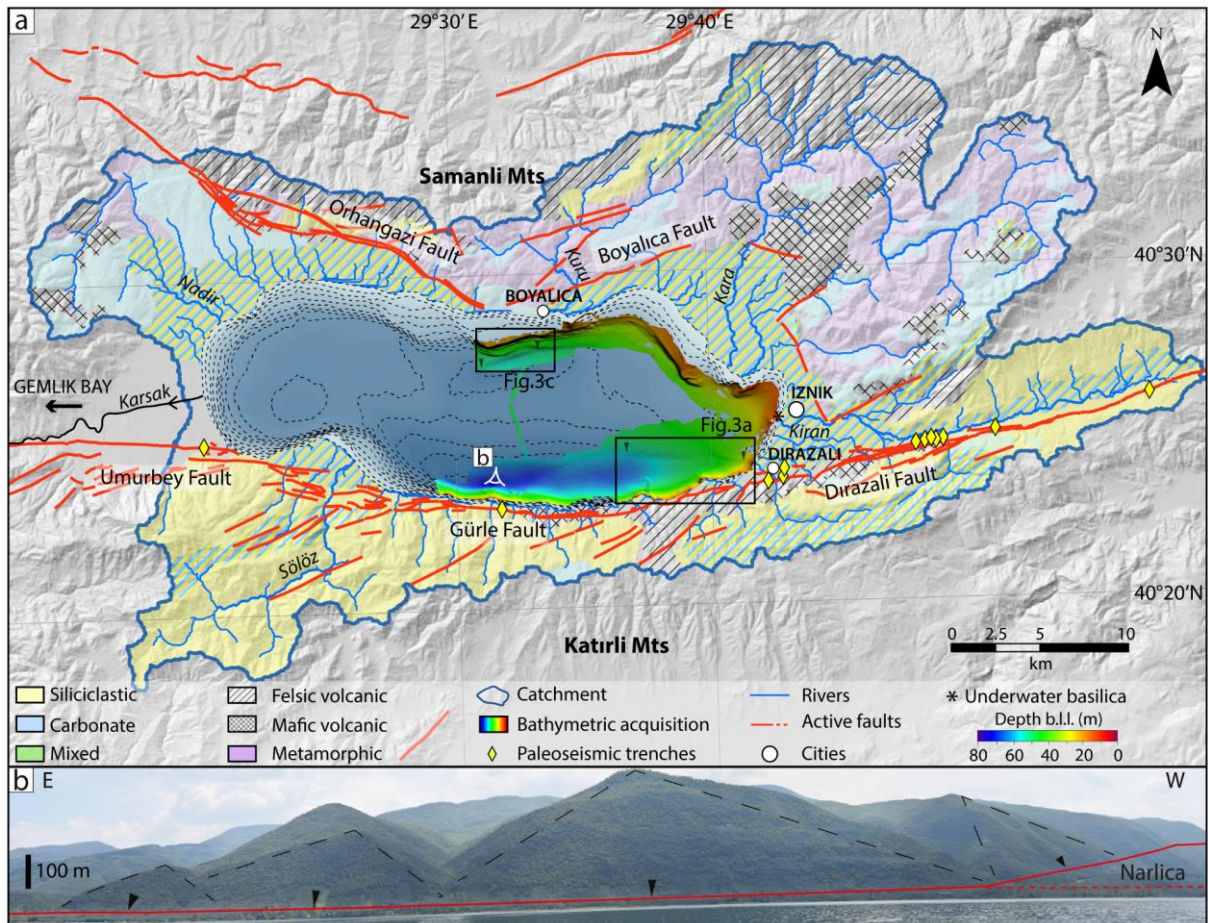
**Fig. 2**: (a) Lithological map of the watershed of Lake Iznik (modified from Viehberg et al., (2012)) and limits of its catchment (dark blue line). The hillshade relief is generated from the SRTM DEM (1 arc-second resolution). The main rivers are drawn in blue. The MNAF and other active faults are represented in red (Öztürk et al., 2009; Doğan et al., 2015; Benjelloun, 2017; Emre et al., 2018). The bathymetric contour lines in the lake represent 5-meter intervals (DSI), superimposed by the hillshaded bathymetry acquired in this study (2 m grid), with a sun illumination angle/elevation of 20°N/45° respectively. A vertical exaggeration of 15 was applied. The color scale represents the depth below lake level (b.l.l.), based on a long-term reference lake level of 83.5 m above sea level. The black arrows show the visible extremities of the two newly discovered faults. The black rectangles indicate the location of **Fig. 3a and c**. (b) Photography of the southern shore of the lake taken from the lake and facing southward, showing triangular facets (black dashed lines) along the Gürle Fault (black arrows). These patterns highlight the significant normal tectonic component in this area.
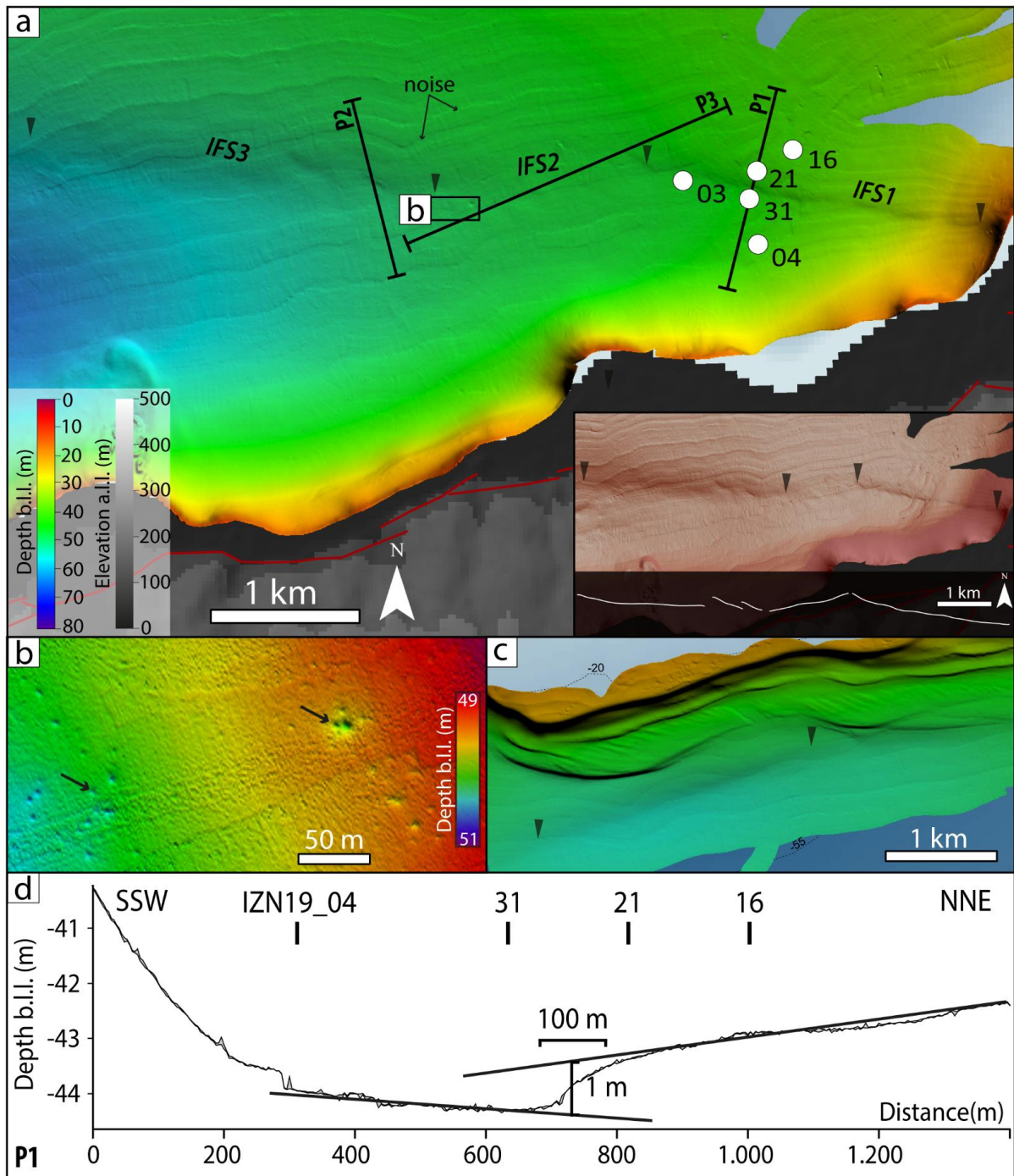
Fig. 3: (a) Hillshaded bathymetric map (5 m grid) of the southeastern part of the lake (Fig. 2 for location). A vertical exaggeration (ve = 20) is applied to highlight the Iznik Fault trace. The black arrows denote the extremities of the different visible segments of the Iznik Fault, termed as IFS1, IFS2 and IFS3 from east to west. White dots represent the core locations (IZN19_03, 04, 31, 21, 16). Black lines indicate topographic P1 (Fig. 3d) and seismic section locations (P2 and P3; Fig. 4). Subaerial elevation is derived from the SRTM model (1 arc-second resolution). The bathymetric and topographic scales are relative to the lake level, below and above (denoted as b.l.l. and a.l.l, respectively). Active faults ashore are shown in red (Benjelloun, 2017;

888    Emre et al., 2018). Inset is an overlay of hillshade and slope maps to emphasize the fault traces. Black arrows

889    indicated the termination of IFS1 and IFS3. In the lower part, an interpretative sketch of the fault geometry

890    is shown. (b) Zoom of the pockmarks along the fault, indicating fluid escapes (1 m grid; ve = 10). Location

891    is shown as a black rectangle in the main figure. (c) Hillshaded bathymetric map of the northern basin,

892    showing the northern lineament, limited by the black arrows (5 m grid; ve = 10; **Fig. 2** for location). (d)

893    Topographic profile P1 derived from the bathymetric data, with a 2-m horizontal resolution and consists of

894    two lines, the min-max values. Core locations are indicating above the profile (IZN19_04, 31, 21, 16). The

895    fault is characterized by a ~ 1 m step on a ~ 100 m-wide area. Hillshaded maps (a, b, c) have a sun

896    angle/elevation illumination of 20°N/45°. Ve increases the noise in the data especially the swath traces.

897
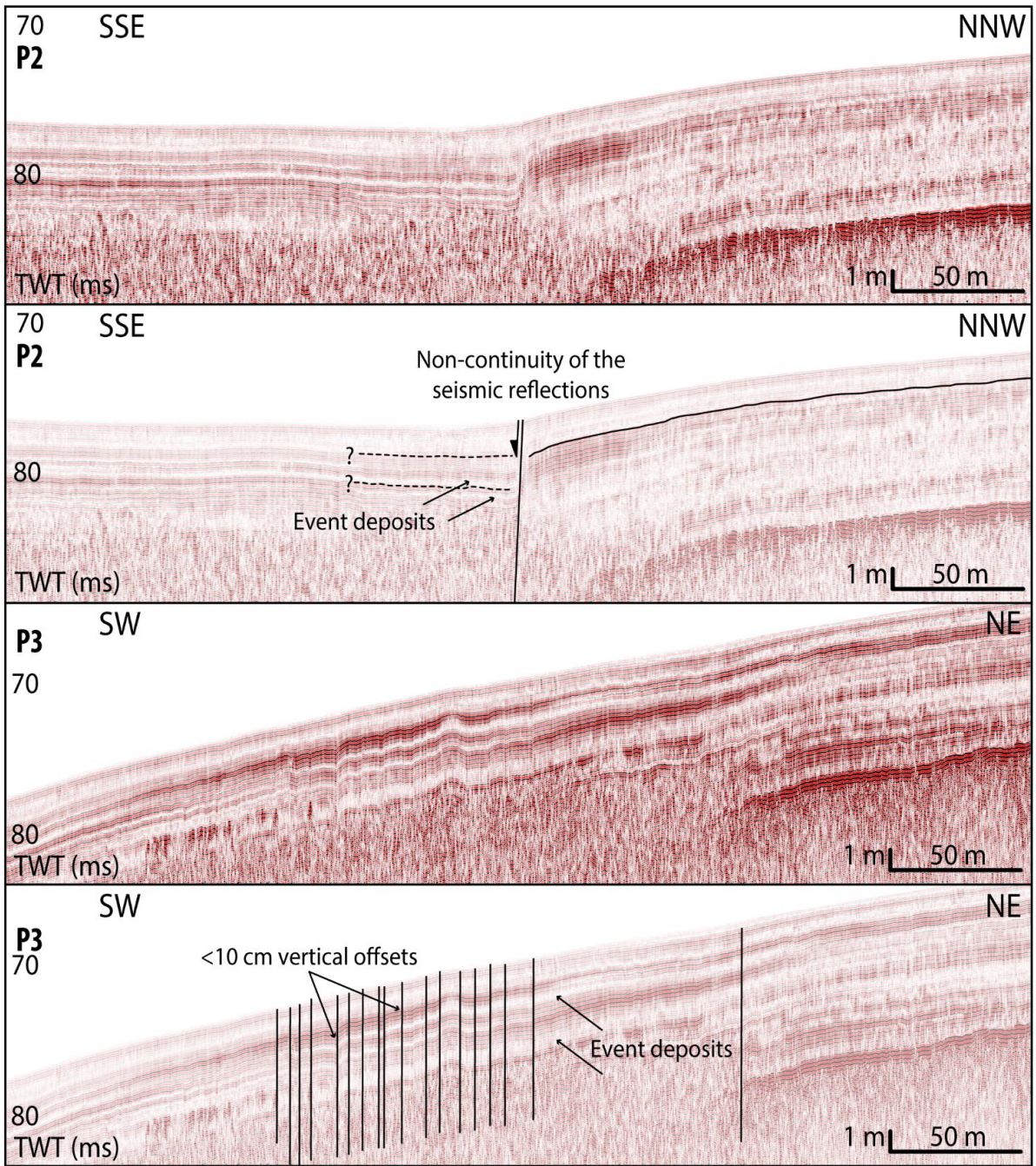
**Fig. 4**: 3.5 kHz single-channel pinger seismic profiles P2 and P3  (locations in **Fig. 3a**). A raw and an

interpreted version is presented for each profile.

900

901 **Fig. 5** (next page): Main sedimentological and geochemical results of IZN19_31 and IZN19_21 cores. (a)

902 Macroscopic description, photography, XRF data (Ti, Ca, Sr, Ca/Sr and Ti/Ca). Ia, Ib, II denote the different

903 facies types, sandy event deposits (Facies IV) are displayed in red. Cl, St, Sd and Pb abbreviations refer to

904 the grain size observations: clay, silt, sand and pebble respectively. The LOI results are presented for the

905 Core IZN19_31 while the grain-size contour plot is displayed for the Core IZN19_21 (b) PCA for cores

906 IZN19_31 and IZN19_21. The respective variables factor maps show that two end-members are defined, one

907 representing the in-lake processes and one corresponding to the terrigenous inputs. The individual factor

908 maps show the correlations of each facies type with the different end members. (c) Detailed coupled

909 SEM/EDS analysis of Facies III versus Facies IV. Optical and SEM photos (left), geochemical mapping

910 (right) show the relative abundance of major elements (Si, Ca, Mg) within the area studied (white box on the

911 SEM photography). The relative oxide compositions between Facies III and IV are shown below.
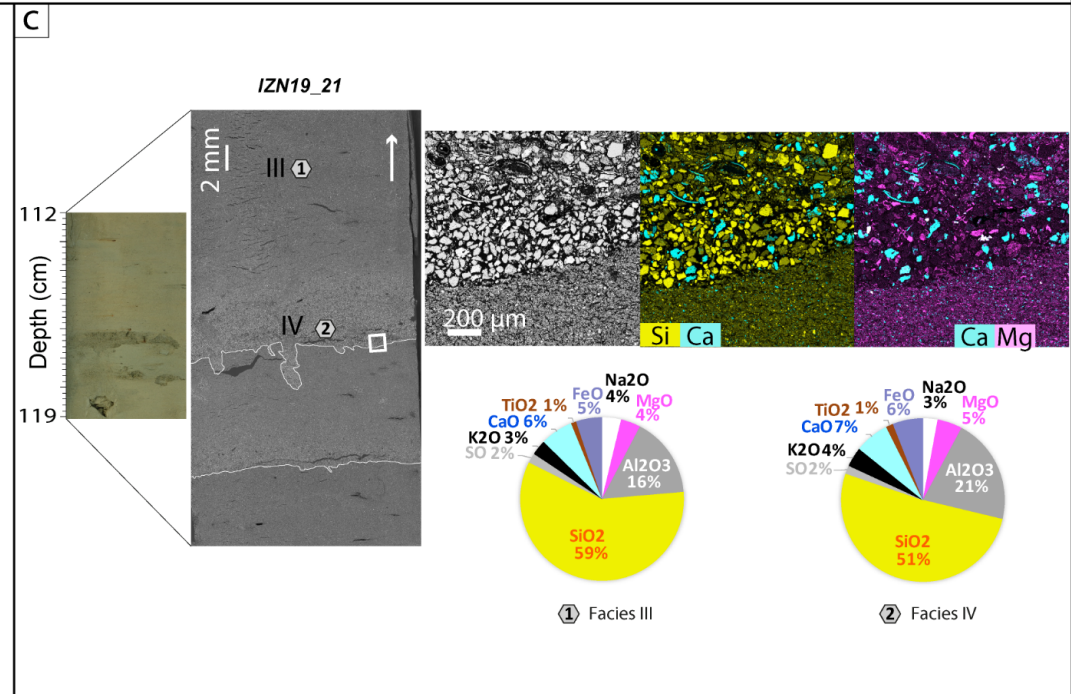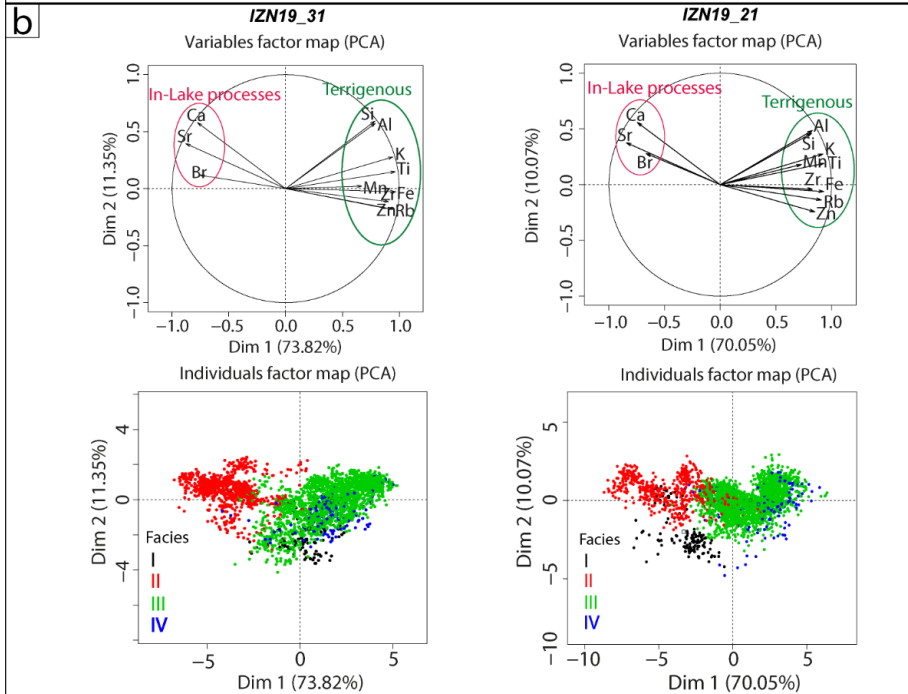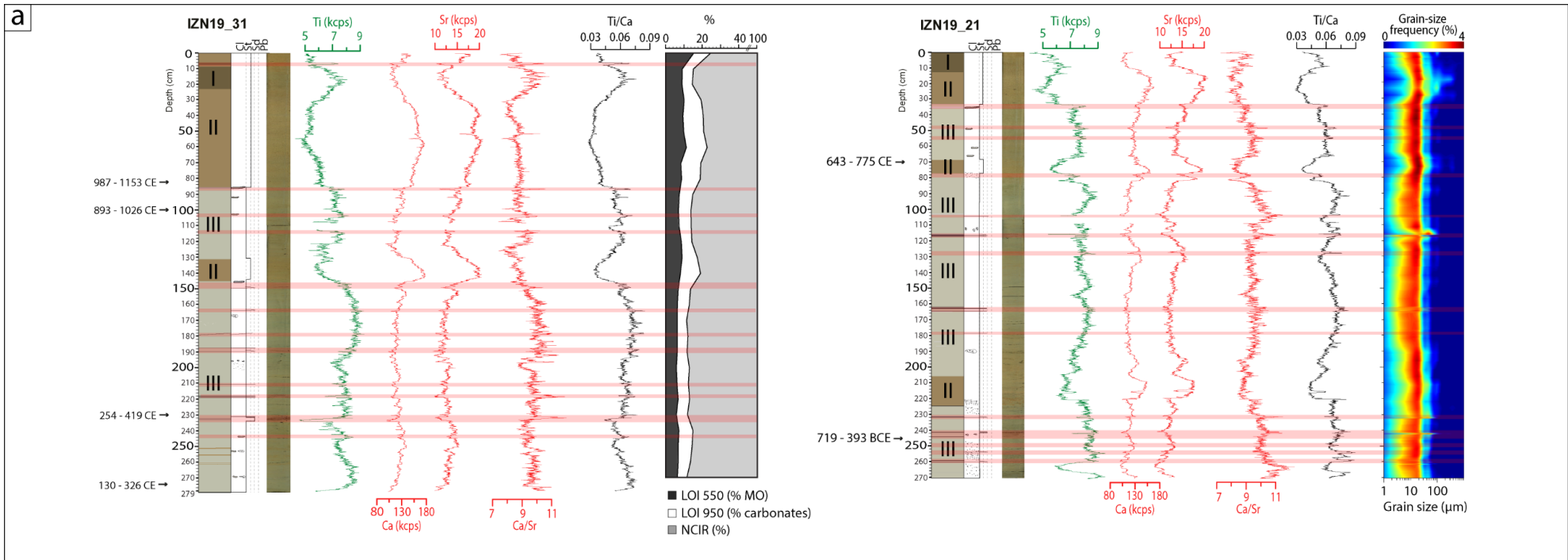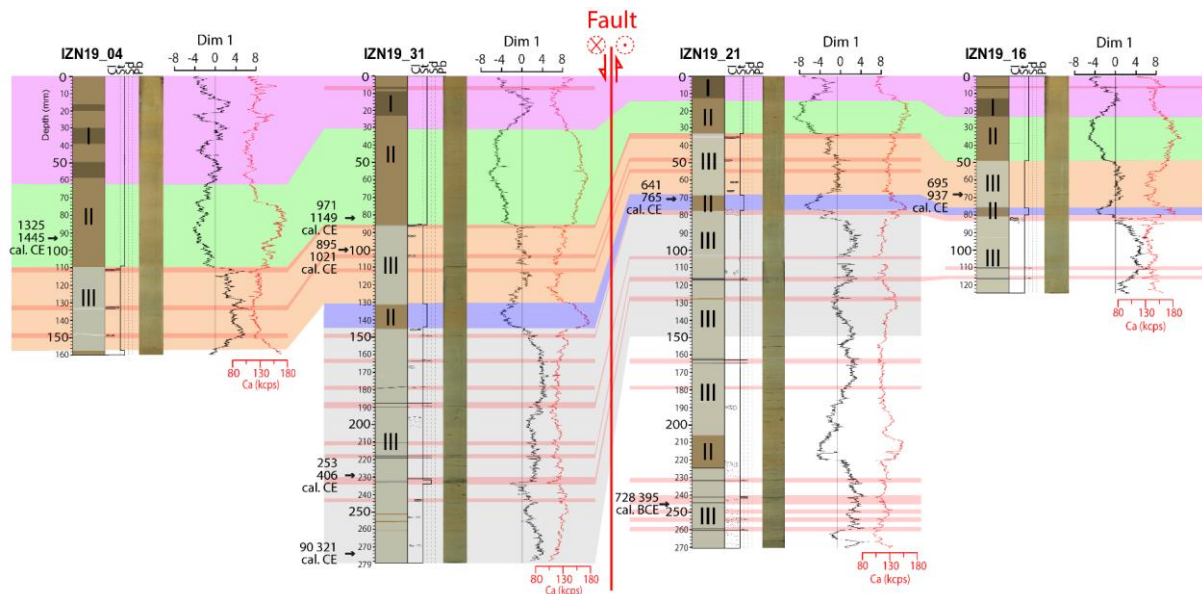
1

2  **Fig. 6**: Core-to-core correlation of the transect across IFS1 (**Fig. 3a**). Topography is neglected. For each core:

3  lithological description, photography, Dim 1 and Ca signal are displayed. The different colors represent five

4  stratigraphic units. Event deposits are shown in red. Individual radiocarbon dates are shown with black arrows

5  (**Table 1** for details). I, II, III represent the names of the different facies types defined in the text.

6
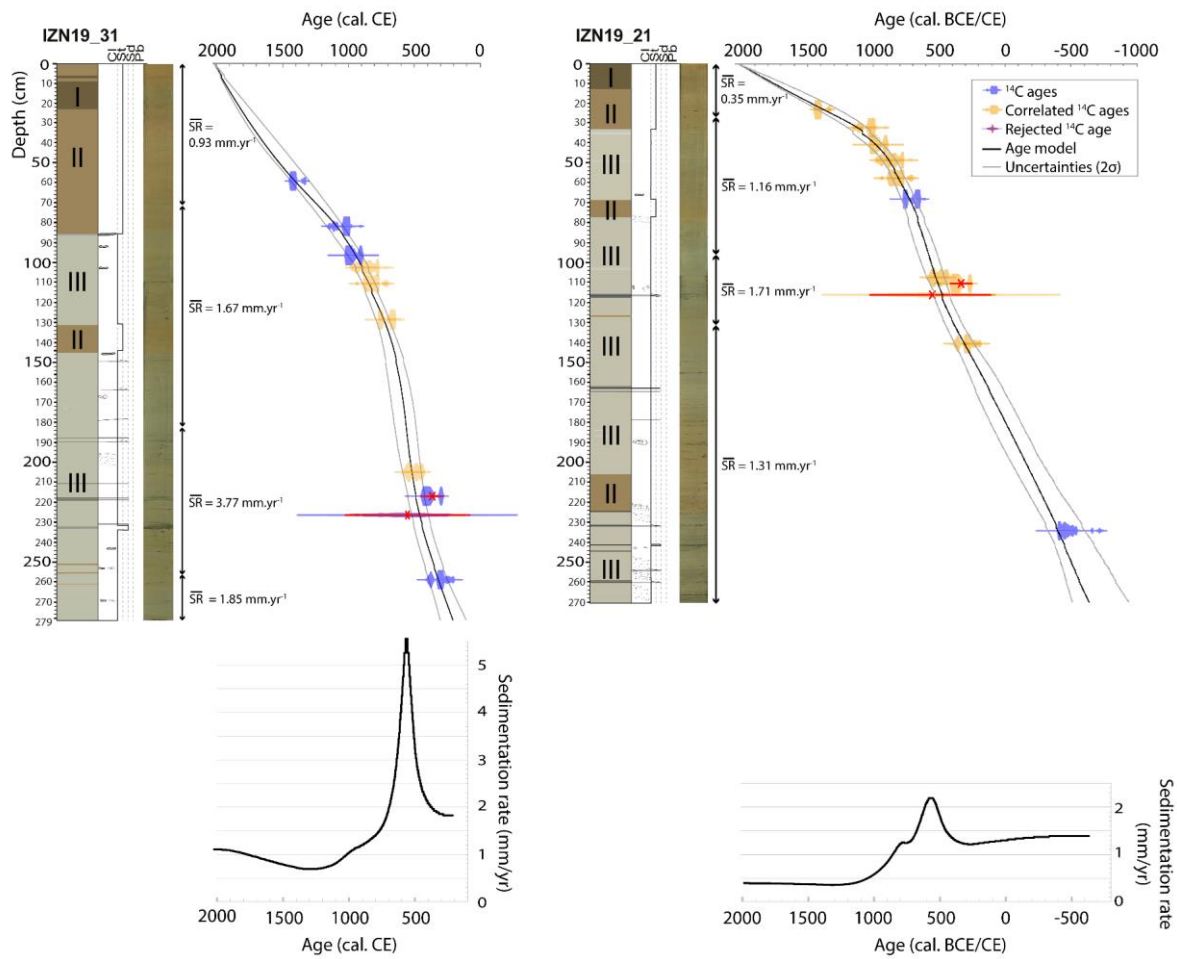
**Fig. 7**: Lithological description, photography, age model for cores IZN19_31 and IZN19_21 and their respective sedimentation rate variation curve through time. The age models are computed with Clam R package (Blaauw, 2010) using the radiocarbon data (**Table 1**). The blue dates origin in the displayed core itself; the orange radiocarbon ages are those which are correlated from other sequences (**Fig. 6**). One radiocarbon age has been rejected for the age model computation due to its large uncertainty (marked in red, details in **Table 1**). $\overline{SR}$ denotes the average sedimentation rate within a given period (refer to the text for details).
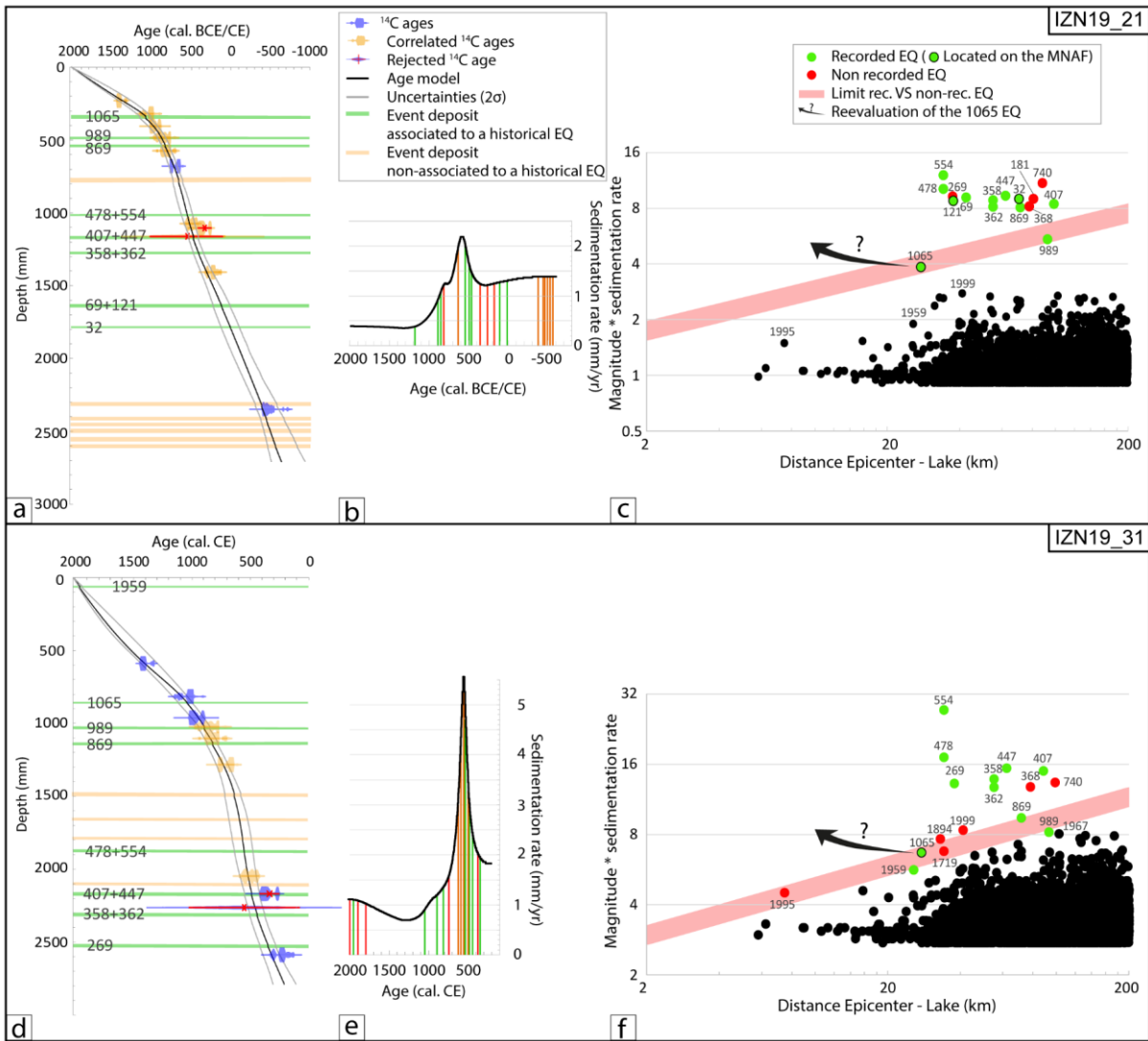
**Fig. 8**: Diagrams displaying for cores IZN19_21 and IZN19_31 (a, d) the interpreted age models. (b, e) The sedimentation rate variations through time. The green lines represent the event deposits associated to an earthquake as opposed to the orange lines. Red lines represent times at which earthquakes happened without event deposit in the sediment cores. (c, f) Conceptual plots presenting the distance of earthquake epicenters to Lake Iznik (40.406N, 29.673E as reference) versus earthquake magnitudes multiplied by the sedimentation rate averaged over the previous 100 years. The red thick line delimits the best fit versus recorded and non-recorded earthquakes. Black dots represent earthquakes below the best fit line that are not recorded in the lake. The black arrows show where the 1065 CE earthquake should be located in the diagram as the Iznik fault ruptured in the lake at that time (see below in the text).

| Core<br>Period | 04 | 31 | 21 | 16 | 03 |
|---|---|---|---|---|---|
| > 1470/1777<br>cal. CE | +44<br>(+275%) | +14<br>(88%) | 16 | +8<br>(+50%) | +4<br>(+25%) |
| > 1000/1154<br>cal. CE | +32<br>(+178%) | +38<br>(+212%) | 18 | +4<br>(+22%) | +12<br>(+67%) |
| > 663/774<br>cal. CE | +12<br>(+33%) | +10<br>(28%) | 36 | -8<br>(-22%) | -2<br>(-6%) |
| > 604/736<br>cal. CE | ? | +3<br>(+33%) | 9 | -4<br>(-44%) | -3<br>(-33%) |
| > 108/306<br>cal. CE | ? | +62<br>(+85%) | 73 | ? | ? |
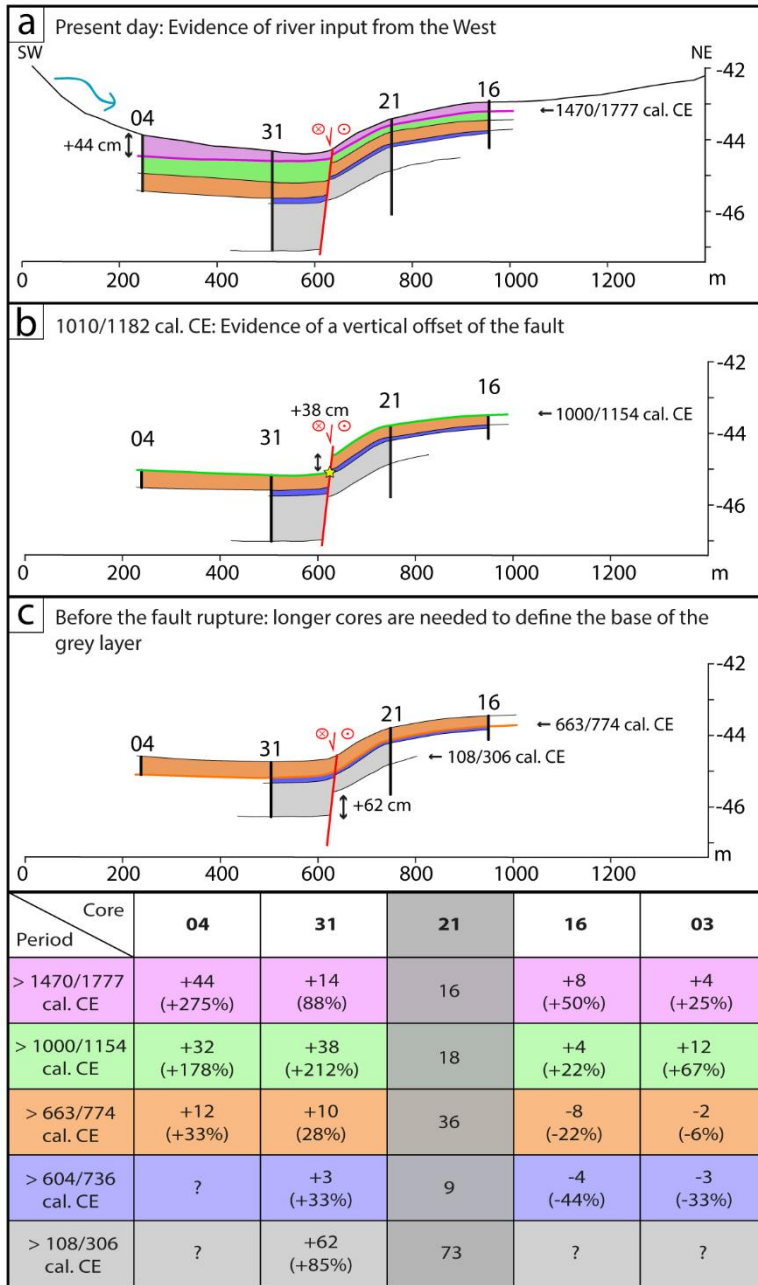
**Fig. 9**: Conceptual diagrams presenting the (paleo)topography and sedimentological reconstructions at three different times. The location of the cores, the distance between each core, their length and the thickness of the different units are drawn to scale. (a) Present day: evidence of river input from the West. The topography is obtained from our bathymetric data (b) at 1000/1154 cal. CE: evidence of a ~ 40 cm vertical offset on the fault (c) before the last fault rupture. The table represents the deviation in sediment thicknesses (in cm) for each core and stratigraphic unit relative to Core IZN19_21. The colors are the same as in **Fig. 6**.
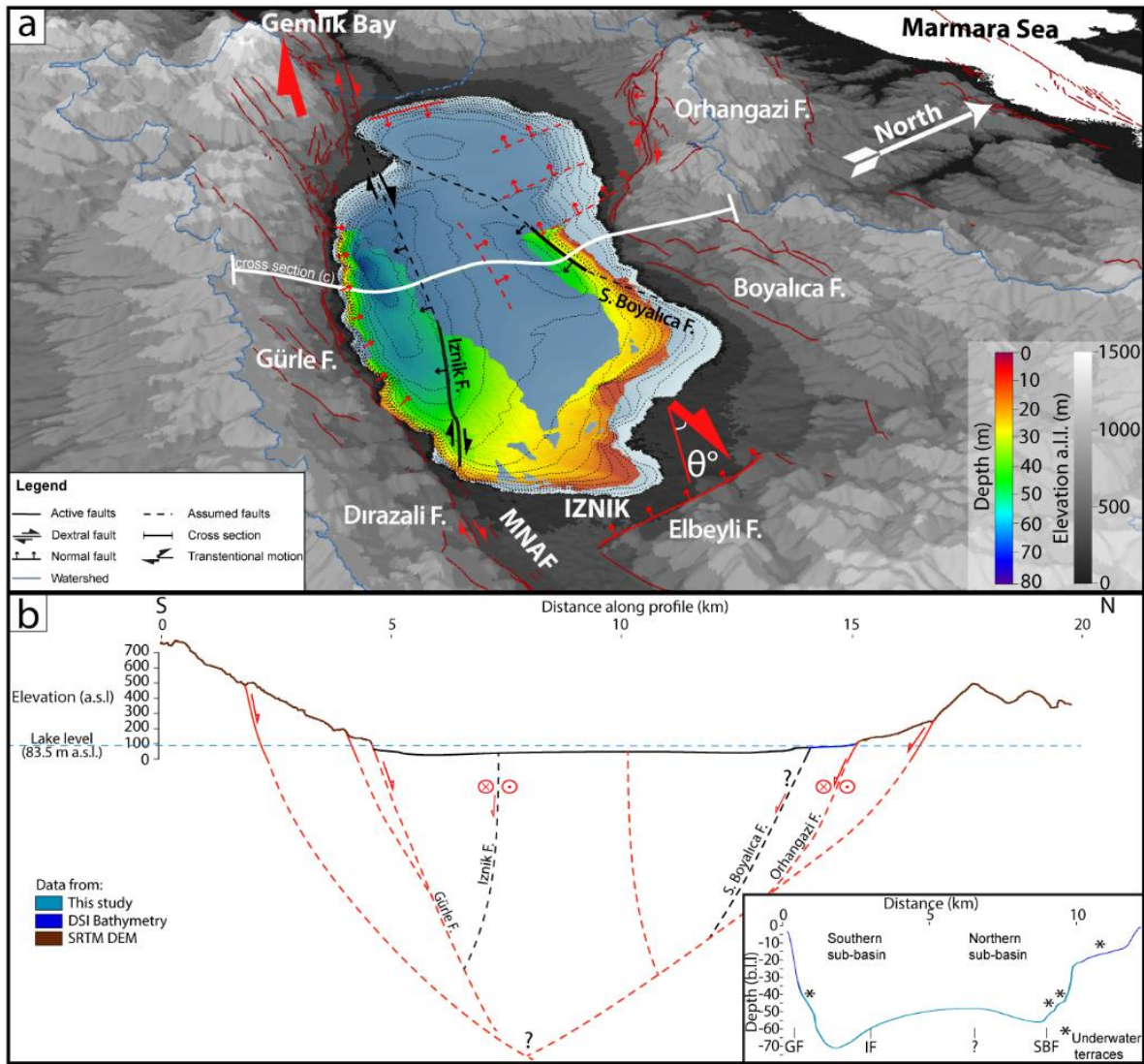
**Fig. 10**: (a) 3D visualization derived from SRTM DEM (1 arc-second resolution) of the Iznik Basin with tectonic interpretation. The bathymetry carried out in this study is superimposed on the DSI bathymetry. The red solid lines are active faults from the literature (Öztürk et al., 2009; Doğan et al., 2015; Benjelloun, 2017; Emre et al., 2018), whereas the red dashed lines represent presumed faults. The black lines represent newly discovered fault structures documented in this study. The blue line represents the limit of the catchment of Lake Iznik. A vertical exaggeration of 3 is applied on each dataset. (b) N-S profile across the lake (see (a) for location), with tectonic interpretation. The black fault lines represent the two faults documented in this study. Inset is a zoom of the lake bathymetry. GF: Gürle Fault; IF: Iznik Fault; SBF: South Boyalıca Fault; *: Underwater terraces.